International Journal of Non-Linear Mechanics 140 (2022) 103907

Contents lists available at ScienceDirect

International Journal of Non-Linear Mechanics

journal homepage: www.elsevier.com/locate/nlm

How surrogates for cortical forces determine cell shape

Jay Stotsky, Hans G. Othmer *

School of Mathematics, University of Minnesota, Minneapolis, MN 55455, United States of America

ARTICLE INFO

Dedicated to Luigi Preziosi on his sixtieth birthday, for his manifold contributions to Mathematical Biology

Keywords:
Cell motility
Helfrich flow
Cellular cortex
Bending modulus
Surface mechanics

ABSTRACT

Recent experimental work has shown that numerous cell types can use different modes to move in different environments. Some cells crawl and some swim, but many can do both, and understanding how they interrogate their environment and determine how to move in response to information acquired is central to understanding basic processes ranging from early development to cancer metastasis. Cell movement usually involves shape changes, which are determined by both intra- and extracellular forces. Intracellular forces are transmitted to the membrane via tractions exerted on the membrane by the cell cortex, a thin composite of actin filaments, motor proteins and various linker proteins underlying the membrane, and herein we determine how surrogates for the normal and tangential components of cortical forces determine the shape of cells.

1. Introduction

Cell shape plays an important role in numerous cell processes, including locomotion, cell division and tissue structure. Locomotion in turn plays an essential role during embryonic development, angiogenesis, tissue regeneration, the immune response, and wound healing in multicellular organisms. Movement is a complex process that involves the spatial and temporal control and integration of a number of subprocesses, including the transduction of chemical or mechanical signals from the environment, intracellular biochemical responses, and translation of the intra- and extracellular signals into a mechanical response. The essential ingredient for motion is that a cell must be able transmit force to its surroundings, and this can be done in many ways [1–3]. While many single-celled organisms use flagella or cilia to swim, there are two basic modes of movement used by eukaryotic cells that lack such structures — mesenchymal and amoeboid. The former, which can be characterized as 'crawling' in fibroblasts or 'gliding' in keratocytes, involves the extension of finger-like pseudopodia and/or broad, flat lamellipodia, whose protrusion is driven by actin polymerization at the leading edge. The amoeboid mode is less reliant on strong adhesion, and cells are more rounded and may employ shape changes to move — in effect 'jostling through the crowd' or 'swimming'. However, recent experiments have shown that numerous cell types display enormous plasticity in locomotion, in that they sense the mechanical properties of their environment and adjust their mode of movement accordingly. Thus pure crawling and pure swimming are the extremes on a continuum of locomotion strategies, but many cells can sense their environment to determine the most effective strategy for moving in that environment. In view of the complexity of the processes involved in different modes, theoretical models are essential for synthesizing what is known to unify observations and for making predictions that can guide further experimental work.

Swimming by protrusions has been analyzed using a 2D model [4], and the results show that *Dictyostelium discoideum* (Dd) cells can swim by propagating protrusions down their body length. The model gives insights into how characteristics of the protrusions such as their height affect the swimmer's speed and efficiency. Moreover, other types of shape changes are also used. Leukocytes can use the mesenchymal mode in the extracellular matrix, but can also migrate *in vivo* without adhering to a surface after adhesion molecules have been knocked out, using a 'flowing and squeezing' amoeboid mode [5]. Simplified theoretical models of such movement have been analyzed to determine how interactions with obstacles affect the motion [4,6].

Protrusions and other shape changes require forces that must be correctly orchestrated in space and time to produce net motion, and to understand this orchestration one must couple the intracellular dynamics with the state of the surrounding fluid or tissue microenvironment. Tension in the membrane and the underlying cortex has emerged as an important factor in the orchestration, and these tensions play a very clear role in some cells. For example, membrane flow that is probably generated by tension gradients can drive amoeboid cell movement [9]. It is also observed that Dd cells can swim without shape changes for several body lengths [10], and this leads to the third mode of amoeboid movement, which is driven by a tension gradient in the membrane [11]. Examples of the morphologies observed in various cases are shown in Fig. 1.

These examples raise a number of interesting questions. For instance, can one predict the balance of forces within a cell needed to

* Corresponding author.
E-mail addresses: jstotsky@umn.edu (J. Stotsky), othmer@umn.edu (H.G. Othmer).

https://doi.org/10.1016/j.ijnonlinmec.2022.103907
Received 2 August 2021; Received in revised form 7 December 2021; Accepted 2 January 2022
Available online 7 January 2022

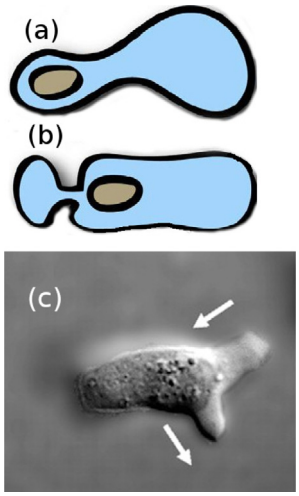

Fig. 1. Two types of stable-bleb morphologies in which the cell movement in confinement is driven by tension gradients. (a) The Ruprecht-type shape, and (b) the Liu-type A2. Reproduced with permission from [7]. (c) A Dd cell moving by retraction of one pseudopod and extension of another.
Source: Reproduced with permission from [8].

produce the various shapes shown in Fig. 1, and to what extent are the shapes fixed by the mechanical feedback from interrogation of the microenvironment of the cell? We address the first of these here by investigating how imposed forces meant as surrogates for cortical forces control the shapes of cells.

1.1. Cortical forces

The membrane of cells is a lipid bilayer ≈10 nm thick that is attached to the cortex, which is 200–300 nm thick (Fig. 2). The cortex is composed of a cross-linked filamentous actin network, embedded with the motor protein myosin-II (myo-II). Myo-II confers rigidity to the network, but can also contract and exert tension in the network. Membrane-bound proteins such as Myo-I – a small motor protein that binds to both actin and the membrane [12] – or linker proteins such as ERMs (ezrin, radixin, and moesin) and talin [13], tether the cortex to the membrane, but the connections are dynamic and the cortical actin filaments are continuously turned over by treadmilling [14]. Both actin turnover and myosin contraction involve ATP consumption, and the result is a dynamic network that can exert normal and tangential forces on the membrane, but can also slide tangentially under the membrane [15,16]. The cortical forces are the primary determinant of cell shape in amoeboid cells [17], and local modulation of cortical mechanics is known to drive cell deformations during cell division, migration, and tissue morphogenesis [18–21]. In many cells these forces generate cell-level flows that are also involved in cell polarization and localization of components involved in shape changes.

A model that incorporates a detailed description of all these factors would be very complex, and the details of the interactions described are not well understood at present. Here we separate the details of cortical structure from the mechanics and simply use a high-level description of the cortex to investigate how cortical forces and heterogeneity of membrane properties determine the shape of cells in quiescent fluids. This enables us to vary the cortical forces directly, irrespective of whether they arise from cortical flows or simply from static tension gradients in the cortex.

Computational results from an earlier 2D model using a free-energy-based description of the membrane show that cells can swim under various combinations of tension gradient in the membrane and heterogeneity of the bending rigidity [11,23]. Moreover the direction of migration depends on the balance between the cortical tension gradient and the variation of the bending rigidity, which may provide an explanation of the observation that some cells move using a small cap in the front, while other cells move with the large bleb in front [24]. The model predicts a cell velocity of 6.0 μm/min when the tension gradient is 10 pN/μm^2, which is consistent with recent experiments. Furthermore, with a suitable spatial variation of the rigidity the cell can evolve to the asymmetric stable-bleb shape, and this also agrees with experimentally-determined values. Overall, the results suggest a solution to the problem raised in [10], and this leads to the third mode of amoeboid movement, which is driven by a tension gradient in the membrane [11].

In this paper we extend these results in several directions. In [11] we studied the individual effects of imposed normal and tangential forces separately, and here the first step is to incorporate them simultaneously in a 3D model so as to understand the effect of their interaction on cell shape. The 2D computations also show that viscous forces on a moving cell have very little effect on the cell shape and thus we focus on the shapes in the absence of movement. Here we find that imposed normal and tangential forces can have opposing effects that can lead to cancellation of their effects on the shape. The degree of deformation in response to normal or tangential forces is generally unequal for similar force magnitudes, with tangential forces producing larger deformations, although this depends on the stiffness of the cell membrane. Imposed normal forces induce changes in the pressure drop across the membrane, and may serve as a surrogate to represent osmotic pressure differences. We also study the impact of variations in the bending and Gaussian curvature moduli. Variation of these quantities can lead to significant shape changes, even in the absence of any applied forces. The computational algorithm used for studying the effects of the forces that arise due to the variable moduli for general 2D surfaces appears to be novel.

As applications of the techniques developed we discuss the influence of anisotropy of active stresses in relation to mitotic furrowing. While the model of furrowing is somewhat simplistic, our results indicate that isotropic tensions are insufficient to cause furrowing, while anisotropic stresses can readily lead to furrow formation. We also show that realistic levels of the applied forces can induce end-to-end pressure differences of the order of 100 Pa within a moving cell, and pressure differences across the membrane on the order of several hundred pascals. Experimentally-measured differences across the membrane range from a few hundred pascals [19] to several thousand [25], depending on the cell type. There is controversy concerning the relaxation of pressure differences following perturbation of a cell [26,27], but we do not address the time-dependent response of the pressure to perturbations.

2. The mathematical model

2.1. The free energy functional and the shape equations

Amoeboid cells have a less-structured cytoskeleton (CSK) than mesenchymal cells, and thus the cell shape is primarily determined by the distribution of internal forces in the membrane and the forces in the cortex. A detailed description of the actin dynamics, myosin motor dynamics, and cortical-network interactions, combined with the transport of actin monomers and other components in the CSK, will be very complex, and to date the most detailed description of the cortex has been as an active gel in simplified treatments [28–30]. While this produces some insights, the biochemical details are embedded in an active component of the stress tensor for the gel, and thus the relative importance of the individual processes involved cannot be investigated. We also do not attempt to develop a detailed model here, but rather, we use an alternate high-level description of the cortex to investigate how cortical forces and heterogeneity of membrane properties determine the shape of cells in quiescent fluids.

The determination of the steady-state shapes of vesicles and red blood cells has been thoroughly studied, both in the absence of fluid

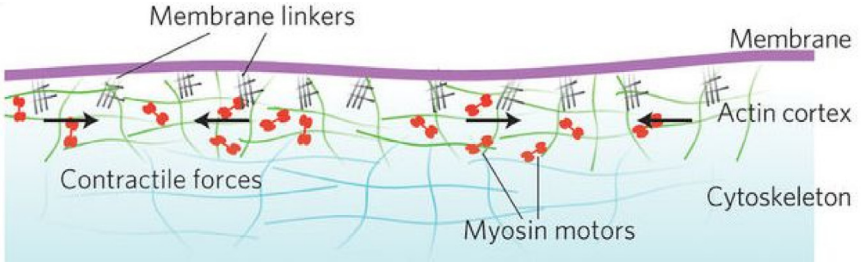

Fig. 2. The plasma membrane (purple) is attached to the actin cortex (green) by linker proteins (black hashes). The cortex is enriched in myosin motors (red), which generate contractile forces. (For interpretation of the references to color in this figure legend, the reader is referred to the web version of this article.)
Source: Reproduced with permission from [22].

motion and in imposed flows [31–35]. In a quiescent fluid the shapes are computed as minimizers of the free energy of the membrane, typically given by a Canham–Helfrich (CH) functional described below, and in a flow they represent shapes that lead to minimum energy dissipation.[1] However, vesicles have no cortical layer and red blood cells have a very thin layer of spectrin – which contains no molecular motors – attached to the membrane. When there is a cortical flow and membrane-cortex tethers are actively formed and broken, there are dissipative processes involved and the membrane-cortex forces are not conservative. Thus we use a virtual work argument to determine stationary shapes in the presence of non-conservative forces.

The membrane has four modes of deformation: dilatation, shear, bending and torsion, but only the bending mode is dominant in most analyses and we follow this practice here. Because a membrane is two-dimensional, it can bend into three-dimensional shapes with variation of the curvature along the membrane, and in addition to the bending energy, which to lowest order is proportional to the square of the local curvature of the membrane, there are contributions to the free energy corresponding to the work associated with area and volume changes when these are conserved.

We let $\Omega \subset R^3$ denote the volume occupied by the cell and let S denote its boundary. We assume that S is a smooth, compact, two-manifold without boundary, parameterized by the map $\Phi : D \subset R^2 \to S$. The position vector $\boldsymbol{x}$ to any material point on the membrane is given by $\boldsymbol{x} = \boldsymbol{x}(u^1, u^2)$ for a coordinate pair $(u^1, u^2) \in D$. We let $\boldsymbol{n}$ denote the outward normal on S and define basis vectors on the surface via

$$\boldsymbol{e}_i = \frac{\partial \boldsymbol{x}}{\partial u^i} \qquad i = 1, 2. \tag{1}$$

The free energy associated with bending, which was first set forth for membranes in [38] and later in [39], has the following form

$$\mathcal{F}_B = \int_S \frac{1}{2} k_c (H - C_0)^2 dS + \int_S k_G K dS \tag{2}$$

where the area element $dS = \sqrt{g} du^1 du^2$, and g is the determinant of the metric tensor $\mathbf{g}$ of the surface. Define κ_1 and κ_2 as the principal curvatures. Then $H = (\kappa_1 + \kappa_2)/2$ is the mean curvature, and $K = \kappa_1 \kappa_2$ is the Gaussian curvature. C_0 is a phenomenological parameter called the spontaneous curvature, k_c is the bending rigidity — which may be stress-dependent [40], and k_G is the Gaussian rigidity, which may also vary over the membrane. When k_G is constant, the integral of the Gaussian curvature is constant if S does not change topological type under deformation, and the integral can be ignored.

To account for applied forces we add the virtual work term $\int_S \mathbf{f} \cdot \boldsymbol{\delta x}\, dS$, where $\boldsymbol{\delta x} = \alpha^i \boldsymbol{e}_i + \beta \boldsymbol{n}$, to reflect the work done by the applied force under an infinitesimal deformation of a reference configuration. Under the constraints of constant surface area A_0 and volume V_0 of the cell, the free energy then takes the form

$$\mathcal{F} = \mathcal{F}_B + \int_S \Lambda \left(\sqrt{g} - \sqrt{g_0} \right) du^1 du^2 + P \left(\int_\Omega dV - V_0 \right) + \int_S \mathbf{f} \cdot \boldsymbol{\delta x}\, dS. \tag{3}$$

[1] In the mathematics literature a functional based on one component of the CH energy leads to the Willmore flow [36,37].

Here g_0 is the determinant of the metric tensor in a reference configuration with area A_0. Λ has units of force/length, which defines a tension, but it is not a surface tension in the usual sense, but rather an in-plane stress of a two-dimensional surface. Further, $P \equiv p_{\text{ext}} - p_{\text{in}}$ is the pressure difference across the membrane, which we assume is constant over the membrane. Typically p_{in} is a few hundred pascals higher than p_{ext} [19]. The constant term PV_0 simply translates the free energy and can be ignored, since it disappears after the first variation of (3) is taken.

A stable equilibrium shape of a cell is a minimizer of $\mathcal{F}$, and thus a solution of $\boldsymbol{\delta}\mathcal{F}/\boldsymbol{\delta x} = 0$ for any infinitesimal deformation $\boldsymbol{\delta x}$ of S. This leads to the following shape equations for the normal and tangential components of the membrane forces.[2]

$$-\frac{\delta \mathcal{F}}{\delta \beta} = -\Delta_s \left[k_c \left(2H - C_0 \right) \right] - k_c \left(2H - C_0 \right) \left(2H^2 + C_0 H - 2K \right) - \bar{\Delta}_s k_G + 2\Lambda H - P + f^n \tag{4}$$

$$\equiv F^n(H, K, P, \Lambda, k_c, k_G, u^1, u^2) + f^n \tag{5}$$

$$-\frac{\delta \mathcal{F}}{\delta \alpha^i} = \frac{1}{2} \left(2H - C_0 \right)^2 \nabla_{s,i} k_c + K \nabla_s k_G + \nabla_{s,i} \Lambda + f_i^t \tag{6}$$

$$\equiv F_i^t(H, K, P, \Lambda, k_c, k_G, u^1, u^2) + f_i^t \qquad i = 1, 2. \tag{7}$$

Here Δ_s, $\bar{\Delta}_s$, and ∇_s are the surface Laplacian and gradient, resp., as defined in Appendix A. In the first equation one sees that Λ enters the normal component via the term $2\Lambda H$, which couples areal distension to the curvature in the normal component of the force. In light of how the variation is defined, the resultant forces are defined per unit area.

We assume hereafter that $C_0 = 0$, and when the bending and Gaussian moduli are constant Eqs (4) & (6) simplify to

$$F^n = -\frac{\delta \mathcal{F}}{\delta \beta} = -2k_c \Delta_s H - 4k_c H \left(H^2 - K \right) + 2\Lambda H - P + f^n \tag{8}$$

$$F_i^t = \nabla_{s,i} \Lambda + f_i^t \qquad i = 1, 2. \qquad i = 1, 2, \tag{9}$$

and these equations have been derived in [41,42] and others. Under constant k_c, k_G, and C_0, the normal component reduces to a generalization of Laplace's law given by

$$p_{in} - p_{ext} = -2\Lambda H - f_n + 4k_c H (H^2 - K) + 2k_c \Delta_s H. \tag{10}$$

When the applied normal component is inward $f_n < 0$ and the applied force elevates the interior pressure. In a cell one contribution to this force can be the osmotic pressure, depending on the cellular environment.

To find the stationary shapes for the free energy we define the pseudo-flow

$$\mu_d \frac{d\beta(u^1, u^2)}{d\tau} = F^n(H, K, P, \Lambda, k_c, k_G, u^1, u^2) + f^n \tag{11}$$

$$\mu_d \frac{d\alpha^i(u^1, u^2)}{d\tau} = F_i^t(H, K, P, \Lambda, k_c, k_G, u^1, u^2) + f_i^t \qquad i = 1, 2. \tag{12}$$

When the cortical forces are incorporated the resulting evolution is no longer a gradient flow, and one simply looks for steady states of (11) and (12), which in general are not minimizers of the CH free

[2] See Appendix A for a sketch of the derivation of these equations.

energy. The quantity μ_d is a drag-coefficient that essentially acts to set the characteristic velocity of the pseudo-flow. We set $\mu_d = \bar{k}T_0/R_0^4 \sim 160\ \mathrm{kg}/(m^2 s)$ where $\bar{k} = 1\times10^{-19}J$, $T_0 = 1s$ and $R_0 = 5\ \mu\mathrm{m}$ are the characteristic energy, time, and length scales. Note that our numerical methods do not directly solve this equation, but rather treat the cell as being imbedded in a viscous fluid. Under the constraints of volume and local area conservation, steady-states of Eqs. (11) and (12) are found directly, or by first imbedding the membrane in a fluid should be equivalent, since in either case, the velocity of the membrane (and surrounding fluid) tends to zero. When f^n and f_i^t are zero, the solutions may be understood as solutions of the Euler–Lagrange equations for the CH functional.

As a characteristic length scale of the problem similar to the ones of vesicles [43] and microswimmers [44,45], we use an effective 3D cell size R_0, which is defined via a sphere of volume equal to the specified volume,

$$V = \frac{4}{3}\pi R_0^3 \tag{13}$$

where V is the specified volume of a cell. The shape equations can be put into dimensionless form by using this characteristic length R_0 and defining a characteristic bending energy $\bar{k}$ (with units of force · length, or equivalently energy). The new * variables are $L^* = L/R_0$, $\Delta^* = R_0^2\Delta$, $k_c^* = k_c/\bar{k}$, $\Lambda^* = R_0^2\Lambda/\bar{k}$, $p^* = R_0^3 p/\bar{k}$, $f^{n*} = f^n R_0^3/\bar{k}$, $f_i^{t*} = f_i^t R_0^3/\bar{k}$ and $\tau^* = \tau/\tau_\mathrm{m}$. For a reference bending energy $\bar{k} = 10^{-19}J$ and a reference radius of $R_0 = 10\ \mu\mathrm{m}$, a dimensionless force equal to 1 corresponds to a dimensional force of $10^{-4}\mathrm{pN}/\mu\mathrm{m}^2$. The resulting shape equations are made scale-free by defining the dimensionless time $\tau^* = \tau/\tau_\mathrm{m}$, where $\tau_\mathrm{m} \equiv \mu_d R_0^4/\bar{k}$ defines a characteristic time unit scaled by a constant characteristic bending rigidity. The resulting forms of (11) and (12) in starred variables are then

$$\frac{d\psi^*(u^1,u^2)}{d\tau^*} = F^{n*}(H^*,K^*,C_0^*,P^*,\Lambda^*,k_c^*,k_G^*,u^1,u^2) + f^{n*} \tag{14}$$

$$\frac{d\alpha^{i*}(u^1,u^2)}{d\tau^*} = F_i^{t*}(H^*,K^*,C_0^*,P^*,\Lambda^*,k_c^*,k_G^*,u^1,u^2) + f_i^{t*} \qquad i=1,2. \tag{15}$$

For reasonable estimates of the parameters τ_m is ~ 0.5 seconds. In the subsequent sections we omit the $*$ notation and assume that quantities are non-dimensional unless otherwise stated.

3. Computational methods

Since the force terms due to bending involve fourth order derivatives of the surface coordinates and are nontrivial to compute, we now discuss the numerical method used to evolve the cell shapes. Further details are given in Appendix B. To solve the governing equations, we use a parametric finite-element method approach to discretize the surface and compute the relevant force terms [46].

The surface is approximated by a triangulation, $\mathcal{T}^h$ consisting of non-overlapping triangles such that each edge is contained in two adjacent triangles, and h is a numerical parameter indicating the size of the triangles. The discretized surface $\mathcal{S}^h$ defined as

$$\mathcal{S}^h = \bigcup_{T_i^h\in\mathcal{T}^h} T_i^h$$

This leads naturally to a piecewise linear approximation of $\mathcal{S}$, however, several advantages of quadratic, or P^2 elements over linear elements for curvature computations were note in [47]. This leads to approximating functions (including the surface position, $\boldsymbol{x}$) in the $\mathcal{P}^2$-Lagrange function space

$$\mathcal{P}^2(\mathcal{S}^h) = \left\{ \boldsymbol{\psi} \in \left[C^0(\mathcal{S}^h)\right]^3 \bigcap \left\{ \left[P^2(T_i^h)\right]^3 \quad \forall T_i^h \in \mathcal{T}^h \right\} \right\}$$

where the superscript 3 refers to the underlying spatial dimension of the Euclidean space $\mathbb{R}^3$. Although the geometry and surface forces are approximated by piecewise-quadratic functions, the resulting description only has C^0 global continuity since derivatives may jump across the edges of triangles. For later use we also define the $\mathcal{P}^2$-Lagrange space of second order tensors:

$$\mathcal{Q}^2(\mathcal{S}^h) = \left\{ \chi \in \left[C^0(\mathcal{S}^h)\right]^{3\times3} \bigcap \left\{ \left[P^2(T_i^h)\right]^{3\times3} \quad \forall T_i^h \in \mathcal{T}^h \right\} \right\}$$

where each component of $\chi \in \mathcal{Q}^2(\mathcal{S}^h)$ is a piecewise quadratic function on $\mathcal{S}^h$. Finally, we found that occasional remeshing was beneficial, and the process for doing this is described in Appendix B.

With these function spaces, the next step is to discretize the nonlinear differential operators defined by $\delta\mathcal{F}/\delta\boldsymbol{x}$. The forces are first split into several terms,

$$\boldsymbol{F} = \boldsymbol{F}_c + \boldsymbol{F}_G + \boldsymbol{F}_A + \boldsymbol{F}_V$$

defined below. The force associated with the mean curvature energy term $k_c(2H - C_0)^2$ will be denoted by $\boldsymbol{F}_c$, the force associated with Gaussian curvature forces by $\boldsymbol{F}_G$, area conservation forces by $\boldsymbol{F}_A$, and volume conservation forces by $\boldsymbol{F}_V$. As discussed below, we also add an additional elastic force, $\boldsymbol{F}_E$ in some cases. The specific forms for these forces are given in the proceeding sections, however, the first step in each case is to obtain a weak form

$$\int_S \boldsymbol{F}(\boldsymbol{x})\cdot\boldsymbol{\phi}\,dS. \quad \forall\boldsymbol{\phi}\in\mathcal{U}^3$$

where $\mathcal{U}$ is a function space (e.g. $\mathcal{H}^1(\mathcal{S})$), and $\boldsymbol{F}(\boldsymbol{x})$ is a weak force[3]. The discretized forces are then found by restricting $\boldsymbol{\phi}$ to $\mathcal{P}^2(\mathcal{S}^h)$, replacing $\boldsymbol{x}$ and $\mathcal{S}$ by $\boldsymbol{x}^h$ and $\mathcal{S}^h$, and replacing any nonlinear terms by their discretized counterparts to yield

$$\int_{\mathcal{S}^h} \boldsymbol{F}^h(\boldsymbol{x}^h)\cdot\boldsymbol{\phi}\,dS \qquad \forall\boldsymbol{\phi}\in\mathcal{P}^2(\mathcal{S}^h).$$

For conciseness, test functions $\boldsymbol{\phi}$ are understood to be elements of $\mathcal{P}^2(\mathcal{S}^h)$ unless otherwise specified in what follows.

We also note that $\mathcal{P}^2(\mathcal{S}^h)$ is a finite-dimensional function space of dimension $N^h = 3n^h$ where n^h is the number of nodal points in the discretization. Therefore, we define a basis. First let $\{\phi_i^h\}_{i=1}^{n^h}$ consist of scalar functions that are equal to 1 at a particular nodal point in the discretization, and zero at all other nodal points. To get a vector basis, define $\boldsymbol{\phi}_{i,k}^h = \phi_i^h\boldsymbol{E}_k$ where $\boldsymbol{E}_k$ is a set of canonical basis vectors in $\mathbb{R}^3$ for $k = 1,2,3$. Thus, we can write

$$\boldsymbol{x}^h(u^1,u^2) = \sum_{i=1}^{n^h}\boldsymbol{x}_i^h\phi_i^h(u^1,u^2) = \sum_{i=1}^{n^h}\sum_{k=1}^{3}x_{i,k}^h\boldsymbol{\phi}_{i,k}^h(u^1,u^2)$$

where $\boldsymbol{x}_i^h$ are the nodal values of $\boldsymbol{x}^h$. In the descriptions below, the weak forms will be written in a continuum rather than discrete sense since the details outlined above are sufficient to convert each into a discrete operator once $\mathcal{S}$ has been triangulated. With these definitions, we also obtain discrete forces

$$\boldsymbol{F}_i^h = \sum_{k=1}^{3}F_{i,k}^h\boldsymbol{E}_k = \sum_{k=1}^{3}\left[\int_{\mathcal{S}^h}\boldsymbol{F}^h\cdot\boldsymbol{\phi}_{i,k}^h\,dS\right]\boldsymbol{E}_k.$$

Before defining the weak forces, we provide typical parameter ranges for the numerical simulations in the following section in Table 1. These are derived from [49,50] with the exception of the shear elasticity modulus, which was chosen heuristically, given that resistance of cell membranes to shear deformation is often much less than their resistance to area change.

[3] For $\phi\in\mathcal{H}^1(\mathcal{S})$, it is natural to consider the weak forces as duality pairings rather than integrals. For any element A in the dual space, $H^{-1}(\mathcal{S})$, we can formally write $A = A_0 + \sum_{i=1}^2 A_i\nabla^i$, for functions $A_0, A_1, A_2 \in L^2(\mathcal{S})$ [48]. Then, the duality-pairing is explicitly given as,

$$\langle A,\phi\rangle = \int_S A_0\phi\,dS + \sum_{i=1}^{2}\int_S A_i\nabla^i\phi\,dS \qquad \forall\phi\in H^1(\mathcal{S}).$$

This type of duality-pairing arises after partial integration. Alternatively, when $\boldsymbol{F}$ is defined in the strong sense, the original integral notation is precise.

Table 1
Typical values of the physical parameters used in the numerical simulations.

Symbol	Value	Dimensionless value	Definition
R_0	5 μm	5	Cell radius
k_c	10^{-19} J	1	Mean curvature modulus
k_G	10^{-19} J	1	Gaussian curvature modulus
E_0	0.01 nN/μm	10	Surface shear elasticity modulus
κ_A	1 nN/μm	1000	Surface area elasticity modulus
$\boldsymbol{f}$	0.1-100 pN/μm^2	1 - 1000	Imposed surface forces
γ	0.01–0.1 nN/μm	1 - 10	Applied tension in mitosis simulations
P	0–100 Pa	0 - 1000	Pressure difference across membrane

3.1. Curvature forces

The first force terms we consider are

$$\boldsymbol{F}_c = -\left(2\Delta_s(k_c H) + 4k_c H(H^2 - K)\right)\boldsymbol{n} + 2H^2\nabla_s k_c \tag{16}$$

which comes from Eqs. (4) and (6) with $C_0 = 0$. Recall that $\nabla_s k_c = (\nabla_{s,i} k_c)\boldsymbol{e}^i$ is a vector term that lies tangent to S at each point. Computationally approximating this force is particularly challenging since if defined in the strong sense, it involves fourth order derivatives of the membrane position, $\boldsymbol{x}$. Rather than directly discretizing the force in Eq. (16), we employ the approach used in [51]. An effective weak form of the forces is obtained by keeping $\boldsymbol{x}$ and a curvature vector $\boldsymbol{H} = 2H\boldsymbol{n}$ as independent variables. In particular, $\boldsymbol{H}$ is defined weakly as

$$-\int_S \nabla_s \boldsymbol{x} : \nabla_s \boldsymbol{\phi} dS = \int_S \boldsymbol{H}\cdot\boldsymbol{\phi} dS \tag{17}$$

Note also that the use of $\boldsymbol{H}$ as an independent variable avoids pitfalls typical of C^0 finite elements that often inhibit the computation of higher order derivatives. A proof of the convergence of this approach is given in [51].

The weak form of $\boldsymbol{F}_c$ is eventually found as

$$\int_S \boldsymbol{F}_c\cdot\boldsymbol{\phi} dS = \int_S \Big[k_c\nabla_s\boldsymbol{\phi} : \nabla_s\boldsymbol{H} - \frac{1}{2}k_c\nabla_s\boldsymbol{\phi}\left(\nabla_s\boldsymbol{x} + \nabla_s\boldsymbol{x}^T\right) : \nabla_s\boldsymbol{H} + k_c\left(\nabla_s\cdot\boldsymbol{\phi}\right)\left(\nabla_s\cdot\boldsymbol{H}\right) + \frac{k_c}{2}|\boldsymbol{H}|^2\nabla_s\cdot\boldsymbol{\phi}\Big] dS.$$

Note that this result is highly nonlinear because the gradient terms ∇_s depend on $\boldsymbol{x}$ via the Christoffel symbols (although these need not be explicitly computed), however, only first order derivatives of $\boldsymbol{x}$ and $\boldsymbol{H}$ are explicitly needed in the computation. While the result in [51] did not consider variable bending moduli, there is nothing in the derivation there that prohibits a variable k_c when the variation in k_c is not a function of the surface geometry, but rather is merely advected as the surface deforms.

Next, let us consider the forces, $\boldsymbol{F}_G$ that result from a variable Gaussian curvature modulus. First, if k_G is constant and no topological changes occur, this term is zero due to the Gauss–Bonnet theorem. When k_G varies, $\boldsymbol{F}_G$ is defined from Eqs. (4) and (6) as

$$\boldsymbol{F}_G = -\left(\overline{\Delta}_s k_G\right)\boldsymbol{n} + K\nabla_s k_G = -\frac{1}{\sqrt{g}}\partial_i\left(\sqrt{g}(2H\delta^i_j - B^i_j)\partial^j k_G\right)\boldsymbol{n} + K\nabla_s k_G.$$

When k_G is variable, we use results from [52] to first compute approximations of the Gaussian curvature and then the complicated modified Laplacian, $\overline{\Delta}_s$, which involves the curvature tensor. Note that $2H = \boldsymbol{H}\cdot\boldsymbol{n}$. Then, the resulting weak form for the force computation is

$$\int_S \boldsymbol{F}_G\cdot\boldsymbol{\phi} dS = \int_S \left(\nabla_s k_G\right)\cdot\left(2H\boldsymbol{I}_s - \boldsymbol{W}\right)\cdot\nabla_s(\boldsymbol{n}\cdot\boldsymbol{\phi}) dS + \int_S K\nabla_s k_G\cdot\boldsymbol{\phi} dS \quad \forall\boldsymbol{\phi}\in\mathcal{P}^2(S^h) \tag{18}$$

where $\boldsymbol{I}_s = \boldsymbol{I} - \boldsymbol{nn}$ is the surface identity, and the second order tensor-valued function, $\boldsymbol{W}$ is an approximation of the Weingarten map, $\nabla_s\boldsymbol{n} = -\boldsymbol{W}$.

This is approximated weakly as

$$\int_S \boldsymbol{W} : \chi dS = -\int_S \nabla_s\boldsymbol{n} : \chi dS = \int_S \boldsymbol{n}\cdot\nabla_s\cdot\chi dS - \int_S \boldsymbol{H}\cdot\chi\cdot\boldsymbol{n} dS, \quad \forall\chi\in\mathcal{Q}^2(S^h)$$

Recall that $\mathcal{Q}^2(S^h)$ is the space of piecewise quadratic second-order tensor-valued functions. The first integral in Eq. (18) can be simplified by integrating against a scalar valued test function ϕ^n. This is possible by noting that $\nabla_s(\boldsymbol{\phi}\cdot\boldsymbol{n}) = \nabla_s\phi^n$ and using the fact that $F^n\boldsymbol{n}\cdot\phi^n\boldsymbol{n} = F^n\phi^n$. The resulting formula yields the weak force,

$$\int_S \boldsymbol{F}_G\cdot\boldsymbol{\phi} dS = \int_S \left(\nabla_s k_G\right)\cdot\left(2H\boldsymbol{I}_s - \boldsymbol{W}\right)\cdot\nabla_s\phi^n dS + \int_S K\nabla_s k_G\cdot\boldsymbol{\phi} dS$$

and in the numerical algorithm, the normal and tangential integral terms are computed separately and then summed to yield,

$$\boldsymbol{F}^h_{G,i} = \left[\int_{S^h}\left(\nabla_s k_G\right)\cdot\left(2H^h\boldsymbol{I}^h_s - \boldsymbol{W}^h\right)\cdot\nabla_s\phi^h_i dS\right]\boldsymbol{n}^h_i + \sum_{k=1}^{3}\left[\int_{S^h} K^h\nabla_s k_G\cdot\boldsymbol{\phi}^h_{i,k} dS\right]\boldsymbol{E}_k.$$

The Gaussian curvature can be approximated by using the identity [52]

$$K = \frac{1}{2}\left(|\boldsymbol{H}|^2 - |\boldsymbol{W}|^2\right)$$

where $|\boldsymbol{W}|$ is the Frobenius norm of $\boldsymbol{W}$. In the discrete setting, this is computed at each nodal point in the discretization, S^h. To our knowledge, the approximation of the forces due to a variable Gaussian bending modulus is novel.

We find that the approximation of K appears to be accurate, and the differential geometry identity for sufficiently smooth genus zero surfaces,

$$\int_S K dS = 4\pi$$

is well approximated in the discrete setting even when the surface S undergoes significant deformation. In future work, it may be worthwhile to consider approximations of $\boldsymbol{W}$ with discontinuous-Galerkin (DG) methods since it involves computing first derivatives of the $\mathcal{P}^2(S)$ basis functions. This was not pursued here for simplicity and because the FEM-software we used does not yet support DG methods.

3.2. Surface area conservation, volume conservation, and surface elasticity

Many cells can only sustain small changes in membrane area before rupturing, while others have membrane reservoirs to accommodate volume changes. In Eqs. (4) and (6), the following forces account for area and volume conservation

$$\boldsymbol{F}_A = 2\Lambda H\boldsymbol{N} + \nabla_s\Lambda$$
$$\boldsymbol{F}_V = -P\boldsymbol{n}$$

While it is possible to formulate numerical methods that conserve volume and area, and treat Λ and P as Lagrange multipliers, we found it easier numerically to allow for small volume and area deviations and

define Λ and P as functions of $\boldsymbol{x}$. Since cells do not precisely conserve volume and area, we believe the approximations detailed below are sufficiently realistic.

To inhibit large changes in surface area under deformation, we modify the energy functional in Eq. (3) as

$$E_A = \int_S \Lambda\left(\sqrt{g}, \sqrt{g_0}\right) \times \left(\sqrt{g} - \sqrt{g_0}\right) dA$$

where $dA = du^1 du^2$ and define a specific form of Λ by

$$\Lambda\left(g, g_0\right) = \kappa_A \frac{\sqrt{g} - \sqrt{g_0}}{\sqrt{g_0}}$$

as in [11], though here in 3D rather than 2D. κ_A is a stiffness coefficient, and if it is large the membrane behaves as though nearly incompressible, whereas if κ_A is small significant area dilatation may occur. To obtain a force, we compute the variation of E_A with respect to the surface shape and find that

$$\int_S \boldsymbol{F}_A \cdot \boldsymbol{\phi} dS = \kappa_A \int_S \left(\frac{\sqrt{g} - \sqrt{g_0}}{\sqrt{g_0}} \right) \nabla_s \boldsymbol{x} : \nabla_s \boldsymbol{\phi} dS.$$

This formulation prevents large changes in global surface area as well as local surface area since $\sqrt{g}$ and $\sqrt{g_0}$ cannot differ by too much at any point on the surface. However, it is sometimes convenient to consider solely global surface area changes. In that case, a similar derivation leads to a force of the form

$$\int_S \boldsymbol{F}_A \cdot \boldsymbol{\phi} dS = \kappa_A \left(\frac{A - A_0}{A_0} \right) \int_S \nabla_s \boldsymbol{x} : \nabla_s \boldsymbol{\phi} dS.$$

where A and A_0 are the current and reference areas of the membrane. An extension of our results might define $\Lambda(g, g_0)$ to be a nonlinear function of g and g_0 to account for effects like membrane folding, although we have not considered that here.

Computational results suggest that in many cases the shapes obtained using resistance to global *vs* local surface area change are not very different, but the tangential deformation patterns that arise in the surface can be quite different. The forces that resist local surface changes are able to balance tangential forces on the surface, thus restricting surface flow, whereas, the global surface area conservation force has no tangential component, and thus allows for significant tangential surface flows.

Volume conservation is imposed weakly via

$$\int_S \boldsymbol{F}_V \cdot \boldsymbol{\phi} dS = \kappa_V (V_0 - V) \int_S \boldsymbol{n} \cdot \boldsymbol{\phi} dS,$$

where V and V_0 are the current and initial volumes, and κ_V is a constant. When κ_V is sufficiently large, volume is conserved to well within 1% during simulations.

In some of our simulations, we also include a simple model of resistance to in-plane shear deformation. For a surface, the deformation gradient is defined as [53]

$$\nabla_{s_0} \boldsymbol{x}(t) = \boldsymbol{e}_i(t) \otimes \boldsymbol{e}^i$$

where summation over $\alpha = 1, 2$ is implied and $\otimes$ indicates a tensor product. Various elasticity tensors can be derived from the deformation gradient, and we use the simple example from [54],

$$\int_{S_0} \boldsymbol{F}_E \cdot \boldsymbol{\phi} dS_0 = -\int_{S_0} E_0 \left(1 - \frac{\sqrt{2}}{|\nabla_{s_0} \boldsymbol{x}(t)|} \right) \nabla_{s_0} \boldsymbol{x}(t) : \nabla_{s_0} \boldsymbol{\phi} dS_0$$

where E_0 is an elasticity modulus and $dS_0 = \sqrt{g_0} du^1 du^2$. Integration over S_0^h is easily done by storing the starting surface, $\boldsymbol{x}^h(0)$. Since $\sqrt{g}$ is approximately conserved, whether we measure forces relative to unit area on S at time t or time 0 is inconsequential (c.f. Theorem 2.6 of [55]). Therefore $\boldsymbol{F}_E$ can be thought of as a force density acting on S at time t. While not studied in detail here, the interaction between curvature and elasticity forces requires further investigation. The presence of elasticity generally makes the membrane stiffer and more difficult to deform.

3.3. Time stepping

With all of the forces defined, the spatially discrete evolution equations are written as

$$\int_{S^h} \frac{\partial \boldsymbol{x}^h}{\partial \tau} \cdot \boldsymbol{\phi} dS = \int_{S^h} \boldsymbol{F}^h(\boldsymbol{x}^h) \cdot \boldsymbol{\phi} dS + \int_{S^h} \boldsymbol{f}^h \cdot \boldsymbol{\phi} dS \quad \forall \boldsymbol{\phi} \in \mathcal{P}^2(S^h). \tag{19}$$

subject to the geometric consistency condition,

$$-\int_{S^h} \nabla_s \boldsymbol{x}^h : \nabla_s \boldsymbol{\psi} dS = \int_{S^h} \boldsymbol{H}^h \cdot \boldsymbol{\psi} dS \qquad \forall \boldsymbol{\psi} \in \mathcal{P}^2(S^h)$$

Unfortunately, we found that after discretizing in time, very small timesteps were required for stability whenever the applied forces were nonzero. Since this restriction remained even when implicit time-stepping was used, a different approach was taken.

Rather than solving the shape equations for the surface evolution to a steady-state, time-stepping was done in a two-stage procedure. We first assume that the membrane is embedded in a viscous fluid, and at each point on the membrane, the velocity is equal to the fluid velocity (denoted $\boldsymbol{V}$),

$$\frac{\partial \boldsymbol{x}(u^1, u^2, t)}{\partial t} = \boldsymbol{V}(\boldsymbol{x}(u^1, u^2), t)$$

The fluid velocity field is obtained by solving Stokes equations with a single-layer potential on S of density $\boldsymbol{F}(\boldsymbol{x})$ at each instant in time. This leads to an abstract evolution equation for the membrane velocity

$$\frac{\partial \boldsymbol{x}}{\partial t} = \int_S \boldsymbol{U}(\boldsymbol{x} - \boldsymbol{y}) \boldsymbol{F}(\boldsymbol{y}) dS$$

where $\boldsymbol{U}$ is the Stokes equation Green's function with a delta-function force. Its explicit form is given in Appendix B.

To obtain a workable numerical method, we expand $\boldsymbol{x}^h$ in terms of the nodal basis vectors,

$$\boldsymbol{x}^h(u^1, u^2, t) = \sum_{i=1}^{n^h} \boldsymbol{x}_i^h(t) \phi_i^h(u^1, u^2)$$

The integration over S is approximated via the Method of Regularized Stokeslets (MRS) [56,57]. This entails replacing the singular kernel $\boldsymbol{U}$ by a regularized kernel, denoted $\boldsymbol{U}_\delta$, and then approximating the single-layer integral via a quadrature method. The regularized kernel is obtained by convolving $\boldsymbol{U}$ with a smooth, radially symmetric function as discussed in Appendix B. Discretizing the time derivative via the forward Euler method leads to an update formula of the form

$$\frac{\boldsymbol{x}_i^{h,n+1} - \boldsymbol{x}_i^{h,n}}{\delta t} = \sum_{j=1}^{n^h} \boldsymbol{U}_\delta(\boldsymbol{x}_i^{h,n} - \boldsymbol{x}_j^{h,n}) \boldsymbol{F}_j^{h,n}$$

where $\boldsymbol{x}^{h,n} = \boldsymbol{x}^h(t_n)$, and the forces at time-step n, $\boldsymbol{F}_j^{h,n}$ are defined as

$$\boldsymbol{F}_j^{h,n} = \int_{S^h} \boldsymbol{F}^{h,n}(\boldsymbol{x}^{h,n}) \cdot \boldsymbol{\phi}_j dS$$

This is essentially a form of mass-lumping since for $\boldsymbol{r} \in \mathbb{R}^3$, we are approximating

$$\int_{S^h} \left[\boldsymbol{U}_\delta(\boldsymbol{r} - \boldsymbol{x}^h) \boldsymbol{F}^{h,n} \right] \cdot \boldsymbol{\phi}_i^h dS \approx \boldsymbol{U}_\delta(\boldsymbol{r} - \boldsymbol{x}_i^h) \cdot \int_{S^h} \boldsymbol{F}^{h,n} \cdot \boldsymbol{\phi}_i^h dS.$$

The most costly aspect of this numerical procedure is the $\mathcal{O}((N^h)^2)$ operations needed to evaluate $\boldsymbol{U}_\delta(\boldsymbol{x}_i^{h,n} - \boldsymbol{x}_j^{h,n})$ for all i and j at each time step. With several thousand points, each time-step takes about 2 seconds on a standard computer or laptop. In the future, improved computational efficiency could be obtained by approximating the summation via a fast algorithm.

While this method appears more numerically stable than direct solution of the shape equations, the time step still must be kept fairly small (on the order of 10^{-5} to 10^{-4} relative to the characteristic time scale). This is due to nonlinearities in the force computation as well as the CFL condition of the forward Euler method. Thus, typical

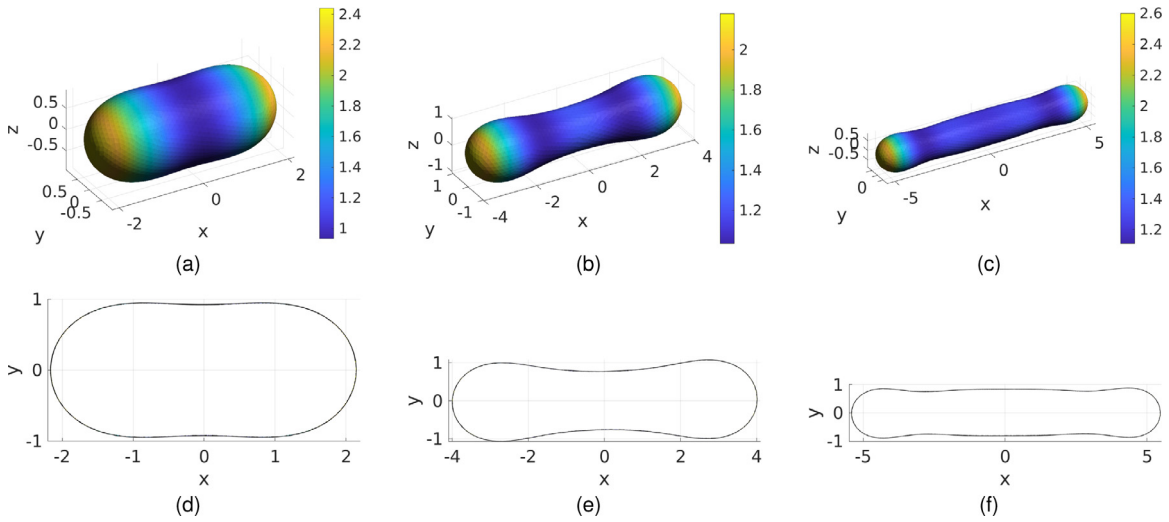

Fig. 3. Equilibrium shapes for prolate spheroids with reduced volumes $\Gamma = 0.85, 0.65, 0.55$, and base parameters otherwise. The color map in this and subsequent figures characterizes the modulus of the mean curvature, with areas of high curvature yellow and low curvature blue. Length units here and hereafter are in μm and curvature in μm^{-1}. Note that the shapes are axisymmetric about the x-axis. The second row consists of the outline of the shapes in the first row. (For interpretation of the references to color in this figure legend, the reader is referred to the web version of this article.)

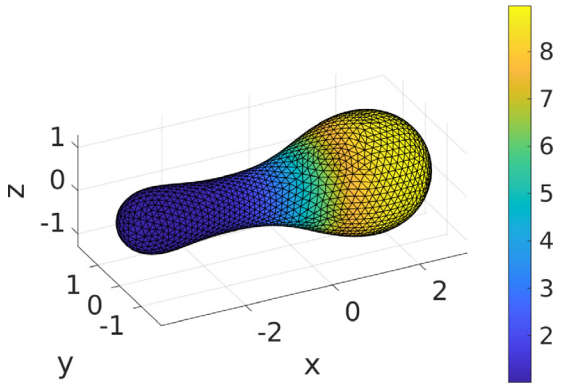

Fig. 4. The spatial variation of k_c when the variation of the bending modulus is $\Delta k_c = 8$.

simulations involve 10^4 to 5×10^4 timesteps and take several hours to a day to run.

To check that the steady-state shapes obtained by the MRS are good approximations of the shape equations, we employed a second stage of the solution procedure where we evolve the discretized shape evolution equations (Eqs. (14) and (15)) starting from the "steady-state" as determined by the MRS. The goal is to check that the viscous interactions inherent in the MRS do not alter the stationary shape significantly.

The advantage of this approach is that the fluid viscosity appears to stabilize the membrane deformations — thus it is computationally easier to evolve the surface according to the MRS. The second stage is primarily a check that a stationary shape has indeed been determined, but these checks can be numerically-expensive since very small time steps are sometimes needed for stability when there are large applied forces on the membrane. Thus the shape equation was only run for a relatively short amount of time in some cases. However, in previous work [23] it was shown that under physiological conditions the effect of fluid on the cell shapes is small, and thus we do not expect that significant shape changes will occur even if such simulations could be extended in time. Because of these considerations, we only used this additional step to test that the resulting shapes (from the MRS simulations) are similar to those obtained by directly solving the shape equations in a few example cases. Larger numbers of simulations are then conducted with the MRS time-stepping to study how the steady-state shapes vary as parameters are changed.

On the other hand, under strong fluid flow, the steady-state shapes can differ significantly from those obtained by the shape equation solution. For instance, red blood cells are known to deform significantly in response to fluid–structure interactions under imposed flows, and thus steady-state shapes found via a shape equation would not apply there.

4. Computational results

In this section we discuss the shapes that result under various prescriptions of the intrinsic and extrinsic properties and forces. As a baseline, we take $k_G = k_c = 1$, $\boldsymbol{f} = \boldsymbol{0}$, $E_0 = 0$, and $\kappa_A = 1000$ as default values of the parameters — all in non-dimensional units. For all objects of a given volume, a sphere has the least surface area, and the combination $V/A^{3/2} = 1/(6\sqrt{\pi})$ is dimensionless. Thus, we define the reduced volume $\Gamma = 6\sqrt{\pi}V/A^{3/2}$ where V and A are the volume and surface area of S. All results herein are obtained computationally, and we begin with the role of intrinsic properties.

4.1. Cell shapes in the absence of applied forces

The simplest case, which serves as a reference case throughout, is obtained when the membrane properties are constant across the surface and there are no applied forces. If the initial shape is a sphere, which has $\Gamma = 1$, it remains spherical, but starting from prolate ellipsoids of varying eccentricity (and hence reduced volume) at $\tau = 0$, the resulting equilibrium shapes are as shown in Fig. 3. As the reduced volume is decreased, pill-like shapes, followed by dumbbell-like shapes result. Even though one of the principal curvatures is negative on the saddles in (b) and (c), the other is large enough to make their sum positive.

In living cells, the cellular cortex need not be distributed evenly, and variations in cortical thickness can occur [24]. We expect that these variations can locally increase or decrease the effective bending moduli of the membrane-cortex system, and we next describe how this is incorporated in our model.

If k_c and k_G vary individually or in concert, significant deviations from these shapes result. In what follows, we prescribe the variation of the moduli in the form $k_c(u^1, u^2) = 1 + \Delta k_c \kappa(u^1, u^2)$, where κ is a scalar-valued surface function with $0 \le \kappa \le 1$, and Δk_c specifies the magnitude of variation (and similarly for k_G). Fig. 4 shows the result

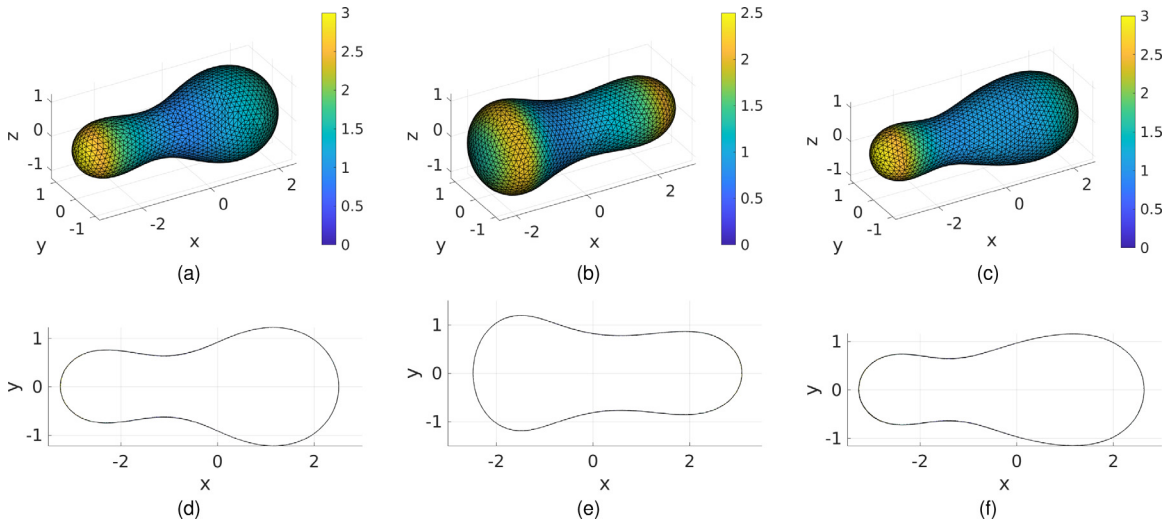

Fig. 5. Changes of shape resulting from a variable k_c and k_G. The top row depicts the equilibrium shape, and the bottom row an outline looking down on the shape. On the left $\Delta k_c = 8$ and $\Delta k_G = 0$, middle has $\Delta k_c = 0$, $\Delta k_G = 8$, and right has $\Delta k_c = \Delta k_G = 8$. In each case, the bending moduli are smallest on the left and largest on the right.

for the case in which k_c varies from 1 at the left end to 9 at the right end.

In Fig. 5 we show the effect of imposing different variations in the bending moduli, with $\Gamma = 0.75$. In this figure we see significant differences in the effect of variation in the bending modulus as compared with the Gaussian curvature modulus. While the form of the forces depends in each case in quite complex ways on the surface geometry, one apparent effect of the bending modulus variation is that the curvature radius increases where the bending modulus is large. In contrast, the Gaussian curvature modulus tends to produce saddle-like regions where one principal curvature is positive and the other negative or close to zero.

An important outcome of these examples is that the shape changes occurring do not depend on any external (*e. g.,* active) forces — they are solely the result of varying intrinsic membrane properties across the membrane. The initiation of motion through variation in membrane mechanical properties may be a means in which cells can move, in addition to the more commonly studied active forces induced by cytoskeletal activity.

4.2. Cell shapes under applied forces

Active forces are also very important for understanding observed cell shapes and the motion of cells. We use surrogates for cortical forces by imposing normal and tangential force fields on the cell membrane, and then compute the corresponding deformation and steady-state shapes. These fields can be normally oriented, tangentially oriented, or some combination of normal and tangential components.

This can be done by computing the normal and tangential vectors at each point on the surface, S and adding forces of the form

$$\boldsymbol{f}^n = f(u^1, u^2)\boldsymbol{n}$$

or

$$\boldsymbol{f}_i^t = f(u^1, u^2)\boldsymbol{e}_i$$

where the function $f(u^1, u^2)$ is a scalar-valued function of the surface coordinates that gives the force strength at each point on the surface. In Fig. 6, this type of force is shown where $f(u_1, u_2)$ is simply a linearly-increasing function from the left to the right of the cell. However, it is not just the applied forces that determine the cell shape, but also how the intrinsic membrane forces interact with the applied forces. In Fig. 7 we show the magnitudes of the different force types at selected points on an axial cross-section curve for a selected set of parameters.

Some results of simultaneously varying normal forces and tangential forces are shown in Fig. 8, where varying levels of the forces are applied to the same starting shape, which is a prolate ellipsoid with $\Gamma = 0.75$. Interestingly, normal and tangential forces seem to have roughly opposite effects on the cell shape. Furthermore, under certain combinations of normal and tangential forces, the shape remains essentially unchanged. It is also noteworthy that tangential force gradients have a greater effect on the cell shape than the normal force gradients, as judged by a comparison of (c) and (g), noting that the tangential force gradient is much shallower than the normal force gradient. This different in sensitivity to normal and tangential forces depends on the magnitude of the bending modulus k_c and on the degree of surface elasticity in the cell membrane, *e. g.,* for a stiffer membrane modulus, E_0, the difference would be reduced (the results in Fig. 8 are for $E_0 = 0$). The normal forces are primarily counteracted by curvature forces, whereas the tangential forces are balanced area-elasticity forces and surface gradients of the bending moduli (if they vary). In Fig. 9, the effect of changing E_0 on a cell with tangential forces is depicted, and we see that larger E_0 leads to less deformation. In a cell, the elasticity modulus may be effected by changes in cross-linking, or the structure of the cytoskeleton, however further investigation of this is needed.

While cell motion and velocity was not studied in detail here, it is a subject of future interest, and we make a few tentative comments about the direction of cell motion due to applied forces. The cell appears to move opposite the side of the cell that has a higher concentration of normal forces, but towards the side that has higher tangential forces. Thus, changing the type of force can potentially lead to changes in the direction of cell motion.

4.3. Surface stresses during mitosis

Aside from the direct application of forces to the cell membrane, it is also useful to think of the applied forces as being derived from stress tensors that represent the cytoskeletal contractility. Given the surface forces one can derive a surface tensor in 2D by the standard Cauchy argument. To study the effect of imposed forces in this framework, we compute the divergence of the resulting stress tensor at each point on the surface. For instance, for an isotropic stress, of the form $\boldsymbol{\sigma}_a = \gamma \nabla_s \boldsymbol{x}$ where γ is the possibly variable surface tensor, we compute the force weakly as a divergence, e.g.

$$\int_S \boldsymbol{f} \cdot \boldsymbol{\phi} dS = -\int_S \gamma \nabla_s \boldsymbol{x} : \nabla \boldsymbol{\phi} dS.$$

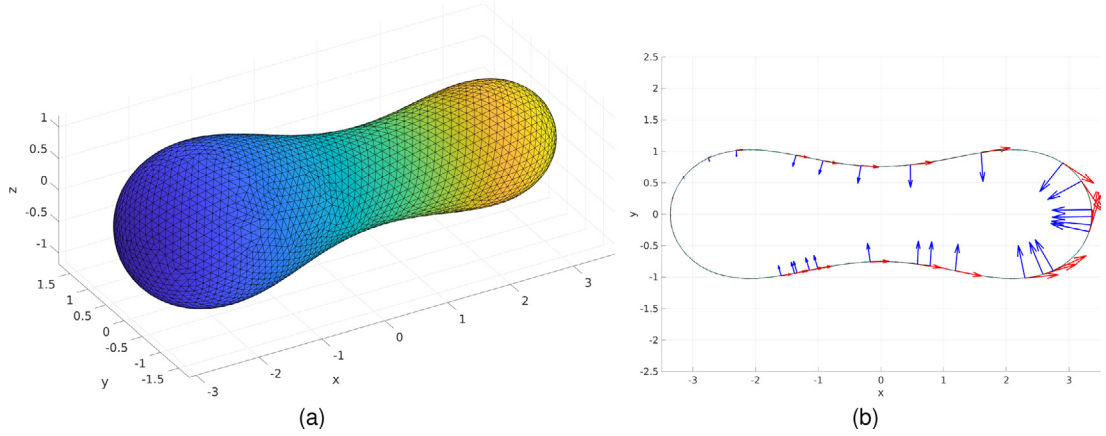

Fig. 6. A depiction of the applied force fields. The norm of the force density under a left-to-right gradient is shown in (a), and in (b) a sampling of the force vectors for normal (blue) and tangential (red) applied forces. In each case the force is zero at the left and is at a maximum at the right. (For interpretation of the references to color in this figure legend, the reader is referred to the web version of this article.)

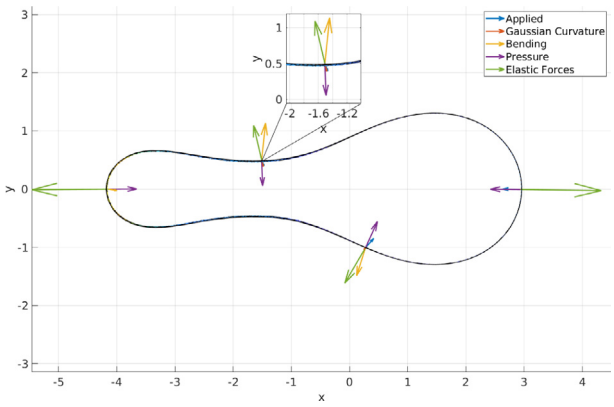

Fig. 7. An illustration of the force balances at several locations along the cell membrane. The applied forces in this figure play a small role in comparison to the other forces.

The same weak-form approach applies even for non-isotropic stresses. As long as σ_a is known, the force can be found via a weak-divergence computation.

As an example, we consider the development of furrows during mitosis. During mitosis, the dividing cell forms a circumferential furrow that contracts inward, eventually leading to the severing of the cell along its mid-line and the formation of two daughter cells. This process occurs in part from the contraction of circumferential cytoskeletal fibers. An interesting result that we have observed is that if these fibers are isotropic on the cell membrane, furrowing does not occur, however, when they are aligned azimuthally, furrowing occurs in proportion to the contractility (measured as a surface tension) of the fibers. In Fig. 10, an image of the mitosis process from a simulation is depicted. Of course, our purely mechanical membrane model is too simple to capture all of the details, and we do not expect the time-course of the process to necessarily reflect reality, nonetheless, this gives some indication of the importance of cytoskeletal fiber orientation during mitosis.

4.4. Intracellular pressure and velocity fields

While the focus of this article is on cell shapes, the use of the Method of Regularized Stokeslets allows for calculation of velocity and pressure fields as well. However, these results are somewhat preliminary since effects such as viscosity contrast viscoelasticity have not been considered.

The pressure Lagrange multiplier in Eq. (3) ensures volume conservation for the enclosed region. For a three-dimensional shape, the bending forces can lead to negative or positive values of P, and surface tension leads to a positive pressure inside the cell relative to the exterior. In the presence of fluid flow, the pressure in the cell can be non-uniform as well. This is particularly of interest in so-called "fountain flows", or internal front-to-back circulation inside the cell (see Fig. 11). Note that for the fluid velocity plot we have used only a global surface area conservation to allow for less restricted surface flow on the membrane.

In response to uniform normal forces, the pressure inside the cell increases with the magnitude of the applied force, as shown in Eq. (10). In a cell the magnitude of pressure change across the membrane is governed by a combination of contractility from the cytoskeleton, osmotic forces from concentration differences, and bending forces. As indicated earlier, the combined effect of the osmotic forces and contractile forces can be modeled by imposing normal forces on the membrane. In the simulations we have conducted, the pressure difference from bending forces is often much smaller than that from the imposed forces, and thus the functional dependence of the pressure drop is essentially a linear function of the applied normal force, as suggested by the generalized Laplace law (10). The computational results are shown in Fig. 12, and the linear relationship exists under a wide range of applied forces. Nonetheless, with no imposed forces one can observe a small pressure drop of order 1Pa across the membrane.

5. Discussion

We have shown how variable bending moduli and the distribution of forces applied to a cell membrane controls the shape of the cell, and how the applied forces determine the direction of movement of a cell. To do this we used a high-level description of the membrane-cortex interaction to facilitate analysis without a detailed model of the cortex. Our aim is to first identify general principles – for example, how does tension affect cell morphology and the intercellular pressure – before developing more detailed models. Progress in this work in this area may have a significant influence on how cell movement is understood, for example in cancer metastasis, and will aid in formulating and testing more detailed models. There are many aspects yet to be investigated, including how the shape affects the swimming speed in a fluid or movement in confined spaces. Thus future work will focus of these problems, first using the high-level description of force used here, and then a detailed model of the cortex and its interaction with the membrane.

There are also interesting unanswered mathematical questions associated with the shape equations. In particular, earlier results have

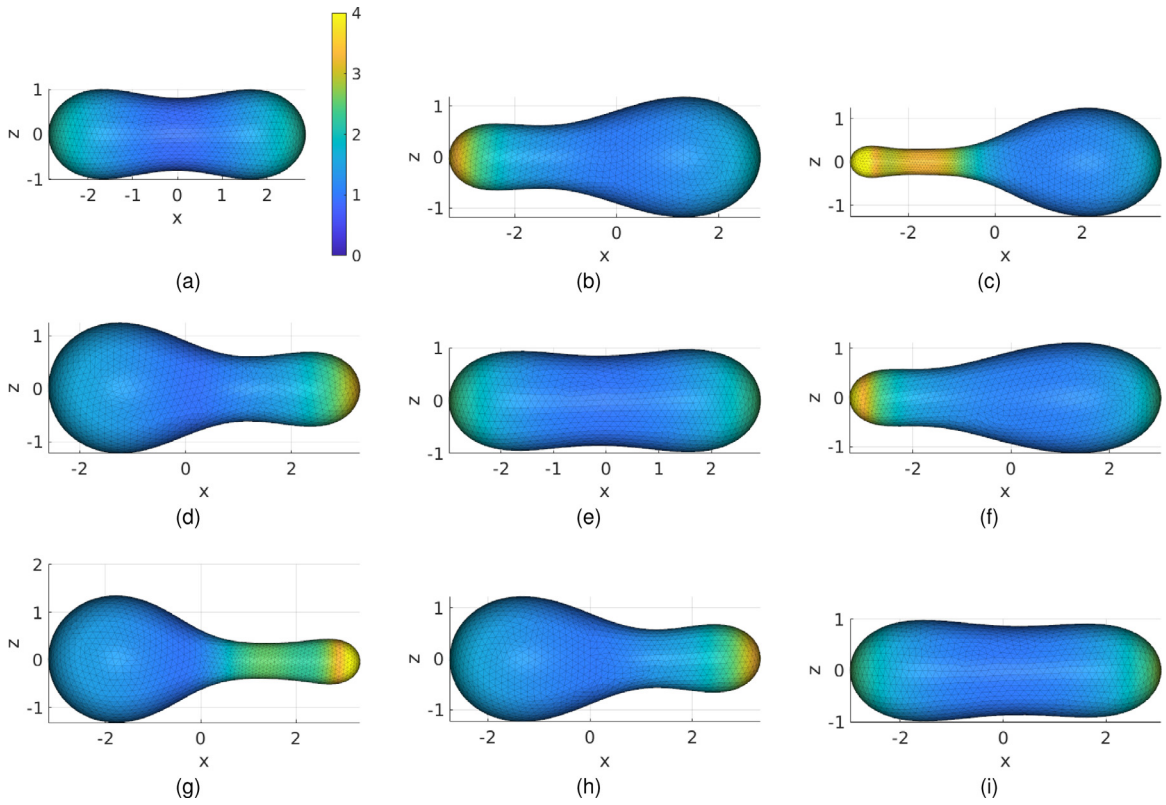

Fig. 8. Cell shapes in response to various combinations of normal and tangential forces at $\Gamma = 0.75$. The left column has f^t equal to 0. The middle column, f^t varies in $(0, 3)$ and on the right f^t varies in $(0, 7)$. The top row has $f^n = 0$, the middle row has f^n varying in $(0, 10)$, and the bottom row has f^n varying in $(0, 25)$. Coloring reflects the curvature (units μm^{-1}). Each image has the same color scale with dark blue corresponding to 0 and bright yellow ≥ 4 μm^{-1}. (For interpretation of the references to color in this figure legend, the reader is referred to the web version of this article.)

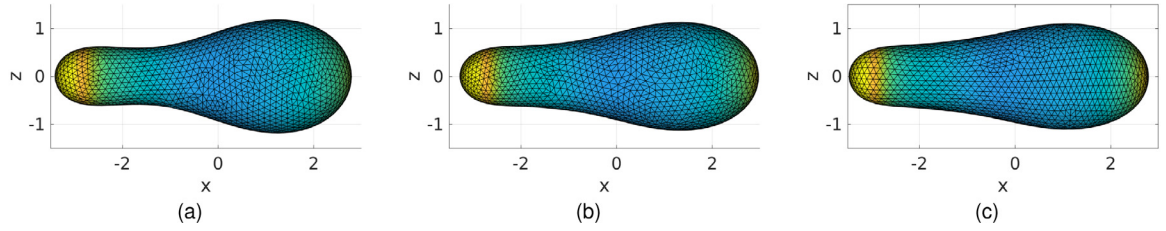

Fig. 9. Effect of increasing E_0 on steady-state shapes. From left to right $E_0 = 0, 50, 100$ and in all cases f^t varies from 0 on the left to 5 on the right, and $f^n = 0$. Notice that the left figure is more deformed compared with the other two.

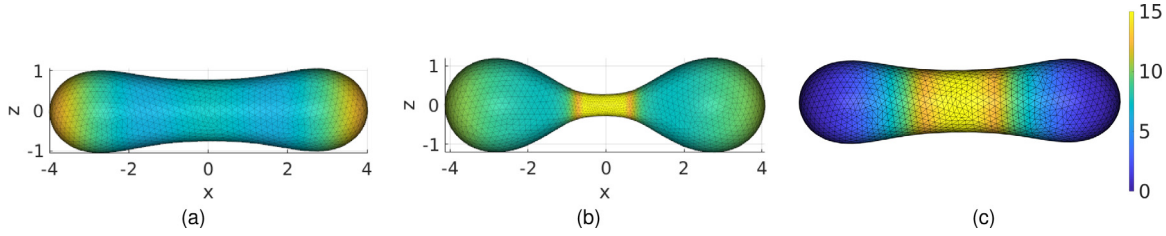

Fig. 10. Simulation of cell mitosis with (a) isotropic tension, and (b) anisotropic tension aligned with a hypothetical fiber orientation to cause constriction of the middle of the cell. Coloring according to the mean curvature. (c) Surface tension distribution in the isotropic case.

found multiple equilibria for a given reduced volume level under Helfrich flow, [31], and we have replicated some of these results computationally. For instance, starting from oblate, rather than prolate ellipsoids, the steady-state shape becomes biconcave as the reduced volume is decreased. In Fig. 13, the evolution, starting from rather complex starting shapes to distinct steady-state shapes at the same reduced volume are shown. In this sense, the apparent non-uniqueness may be the result of projecting a higher dimensional manifold of shapes onto a single parameter. For instance, if one includes both reduced volume and the starting shape, then the non-uniqueness apparently vanishes. It would be interesting to determine what types of starting shapes lead to different equilibria. In future work, many extensions could be made to attempt to study this non-uniqueness in the context of applied forces as well. Detailed phase diagrams have been computed when there are no applied forces [31], but much remains to be done to fully understand how external forces can alter the steady-state shapes.

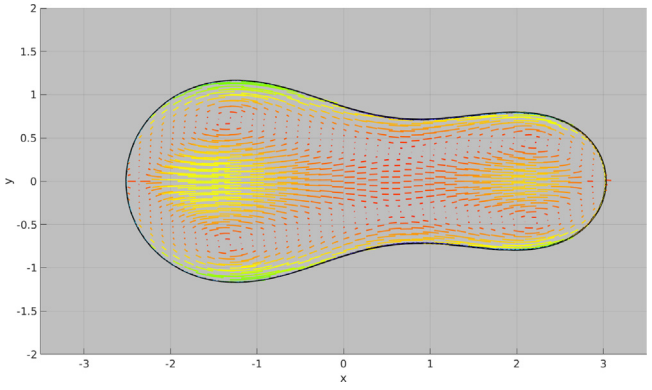

Fig. 11. Depiction of a fountain flow circulation within a cell. The velocity field shown is obtained using the MRS. The largest velocities are on the order of 10 μm/s.

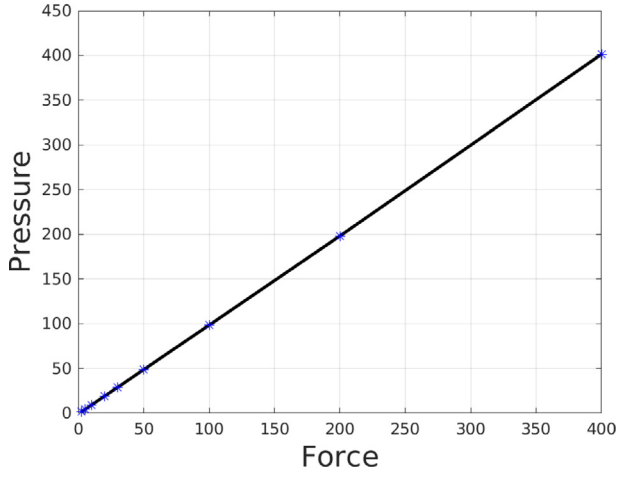

Fig. 12. Mean pressure drop as a function of a uniform applied normal force. Note that the y-intercept is near, but not quite at zero due to some residual pressure drop from the bending forces. The blue asterisks represent pressure drops from individual simulations and the black curve is merely connecting the dots. Units for the force-density and pressure are pN/μm^2.

CRediT authorship contribution statement

Jay Stotsky: Writing – original draft, Writing – review & editing, Software, Methodology, Formal analysis. **Hans G. Othmer:** Writing – original draft, Writing – review & editing, Conceptualization, Methodology, Supervision, Funding acquisition.

Declaration of competing interest

The authors declare that they have no known competing financial interests or personal relationships that could have appeared to influence the work reported in this paper.

Acknowledgments

This work was supported in part by NSF, United States Grant DMS 1311974, NIH, United States Grant 54-CA-210190, the Isaac Newton Institute, United Kingdom, and the Simons Foundation, United States.

Appendix A. Summary of the derivations

Notation and basic quantities

A smooth surface $S \subset R^3$ will be parameterized by $u = (u^1, u^2)$ and the position vector in R^3 to the surface is denoted $\boldsymbol{x}(u)$. The surface tangent vectors (which may be nonunitary) at each point on the surface are defined by the parametric derivative of $\boldsymbol{x}$ with respect to the surface coordinates, namely,

$$\boldsymbol{e}_i(u^1,u^2) = \frac{\partial \boldsymbol{x}}{\partial u^i}(u^1,u^2) \qquad i = 1,2$$

and the surface normal $\boldsymbol{n}$ is defined by the relations $\boldsymbol{n}\cdot\boldsymbol{e}_i = 0, \quad \boldsymbol{n}\cdot\boldsymbol{n} \equiv \langle \boldsymbol{n},\boldsymbol{n}\rangle = 1$. The covariant metric tensor of the surface is defined as $g_{ij} = \boldsymbol{e}_i\cdot\boldsymbol{e}_j$, the contravariant surface metric tensor is the inverse tensor defined by the relation $g_{ij}g^{jk} = \delta_i^k$, and the determinant of g_{ij} is denoted by $g \equiv det(g_{ij})$. Here and hereafter a repeated upper and lower index denotes summation.

The Levi-Civita symbol is defined in covariant and contravariant form as

$$\epsilon_{ij} = e_{ij}\sqrt{g}$$
$$\epsilon^{ij} = e_{ij}/\sqrt{g}$$

where $e_{12} = -e_{21} = 1$ and $e_{11} = e_{22} = 0$.

The second derivative of $\boldsymbol{x}$ is given by Gauss' formula

$$\boldsymbol{e}_{i,j} \equiv \frac{\partial^2 \boldsymbol{x}}{\partial u^i \partial u^j} = \Gamma_{ij}^k \boldsymbol{e}_k + B_{ij}\boldsymbol{n},$$

where $\boldsymbol{n}$ is the outward normal to the surface and the factor Γ_{ij}^k is called a Christoffel symbol and is defined as

$$\Gamma_{ij}^k = \boldsymbol{e}^k \cdot \frac{\partial \boldsymbol{e}_i}{\partial u^j}.$$

This is a surface directional derivative in the direction of $\boldsymbol{e}_i$, where $,i$ denotes the derivative with respect to u^i. The components of the surface curvature tensor B are defined as

$$B_{ij} = \boldsymbol{n}\cdot\boldsymbol{e}_{i,j} = -\boldsymbol{n}_{,j}\cdot\boldsymbol{e}_i.$$

Weingarten's equation relates the variation of the normal to the curvature tensor via

$$\boldsymbol{n}_{,i} = -B_i^j \boldsymbol{e}_j.$$

The mean curvature is $H = \frac{1}{2}B_i^i$, and the Gaussian curvature is given by $K = det(B_\cdot^\cdot)$.

Derivatives in the direction of the tangent vectors or their dual are called covariant derivatives. The components of the covariant derivative of a co- and contravariant vector $\boldsymbol{w}$ defined on S are

$$\nabla_{s,j}(w_i) \equiv \frac{\partial w_i}{\partial u^j} - w_k\Gamma_{ij}^k \qquad \text{and} \qquad \nabla_{s,j}(w^i) \equiv \frac{\partial w^i}{\partial u^j} + w^k\Gamma_{kj}^i,$$

where in each case the second term accounts for the variation of the basis on the surface, and the set $\{\boldsymbol{e}^i\}$ is the dual basis to $\{\boldsymbol{e}_i\}$. This leads to definitions of the gradient and divergence of a vector field on S as follows. Hereafter we consider only contravariant vectors and define $\nabla_s \equiv \boldsymbol{e}^i\nabla_{s,i}$; then the surface gradient of a scalar is the standard parametric gradient

$$\nabla_s F = (\nabla_{s,i}F)\boldsymbol{e}^i$$

and the surface gradient of a vector is

$$\begin{aligned}\nabla_s \boldsymbol{F} &= \nabla_{s,i}(F^j\boldsymbol{e}_j + F^n\boldsymbol{n})\boldsymbol{e}^i \\ &= F^j_{;i}\boldsymbol{e}_j\boldsymbol{e}^i + F^n_{;i}\boldsymbol{n}\boldsymbol{e}^i + F^n\boldsymbol{n}_{;i}\boldsymbol{e}^i + \boldsymbol{e}j;iF^j \\ &= \left(F^j_{;i} - F^nB_i^j\right)\boldsymbol{e}_j\boldsymbol{e}^i + \left(F^n_{;i} + F^jB_{ji}\right)\boldsymbol{n}\boldsymbol{e}^i.\end{aligned}$$

where a semicolon denotes the covariant derivative, *i.e.*, $\nabla_{s,i}w^j \equiv w^j_{;i}$.

The divergence of a vector field is given by

$$\nabla_s\cdot\boldsymbol{F} = \nabla_{s,i}(F^j\boldsymbol{e}_j + F^n\boldsymbol{n})\cdot\boldsymbol{e}^i = F^j_{;j} - F^nB_i^i = F^i_{;i} - 2HF^n$$

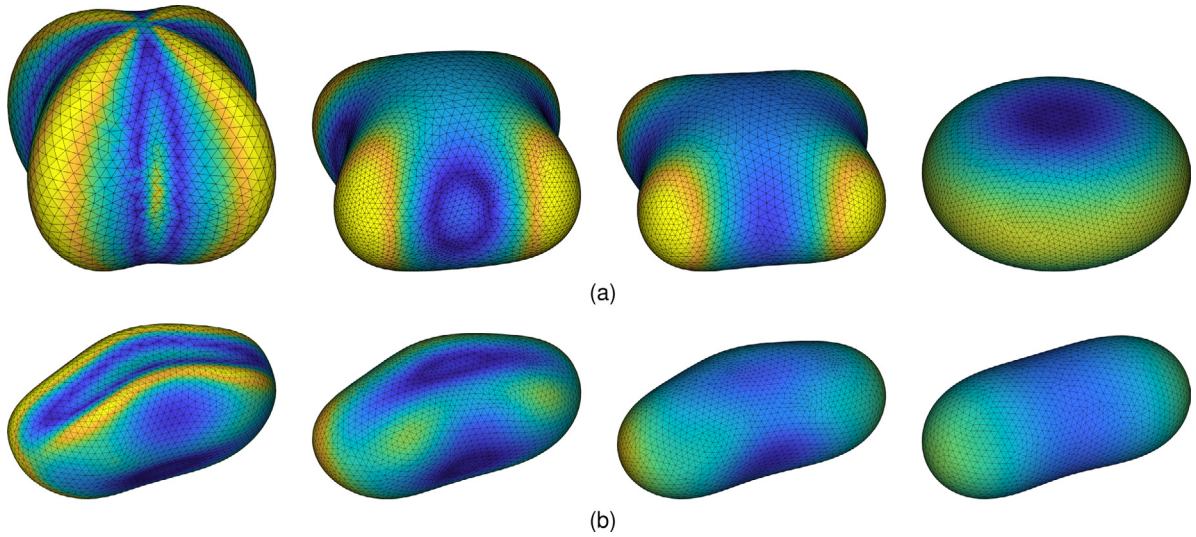

Fig. 13. Evolution to steady-state shapes under Helfrich flow for two different, radially asymmetric starting shapes. In (a) the steady-state is oblate with $\Gamma \approx 0.87$ and in (b) the steady-state is prolate with $\Gamma \approx 0.85$. Coloring is according to $|\boldsymbol{H}|$ which has a maximum value around 5 μm^{-1} in both simulations. (For interpretation of the references to color in this figure legend, the reader is referred to the web version of this article.)

In particular we have

$$\nabla_s \cdot \boldsymbol{n} = \nabla_{s,i}\boldsymbol{n} \cdot \boldsymbol{e}^i = -B_i^j \boldsymbol{e}^i \cdot \boldsymbol{e}_j = -B_i^i = -2H$$

An important and related result is the surface divergence theorem. This can be stated for closed surfaces as

$$\int_S \nabla_s \cdot \boldsymbol{F} dS = \int_S -2H\, \boldsymbol{F} \cdot \boldsymbol{n}\, dS$$

in terms of how we have defined $\boldsymbol{n}$ and H. From this, a surface Green's identity (partial integration formula) may be obtained:

$$\int_S \nabla_s \cdot (\psi \boldsymbol{F})\, dS = \int_S \psi \nabla_s \cdot \boldsymbol{F} + \boldsymbol{F} \cdot \nabla_s \psi dS = -\int_S 2H\, \psi \boldsymbol{F} \cdot \boldsymbol{n} dS.$$

Another related result for smooth scalar fields F is

$$\int_S \nabla_s \cdot \nabla_s F\, dS = 0$$

since $\nabla_s F$ has no normal component. Note that for arbitrary $\boldsymbol{F}$ and ψ, these integration formulas are only correct on closed surfaces. However, since cell membranes are typically closed surfaces, we do not encounter any open surfaces in this article.

Deformation of a surface of fixed free energy

In seeking a stable shape of a cell under imposed forces we look for surfaces of minimum free energy as stationary surfaces of the evolution equations for surface variations. To derive the evolution equations we impose an infinitesimal deformation of the surface by imposing an infinitesimal change in the position vector to any point on the surface in the form

$$\delta \boldsymbol{x} = \alpha^i \boldsymbol{e}_i + \beta \boldsymbol{n}.$$

This induces changes in the factors that characterize the surface, such as the tangent vectors, the area, etc. Those needed for the variation of terms in the energy are as follows.

$$\begin{aligned}
\delta \mathbf{e}_j &= \left(\nabla_{s,i}\alpha^k - \beta B_j^k\right)\mathbf{e}_k + \left(\beta_{,j} + \alpha^k B_{kj}\right)\mathbf{n},\\
\delta \mathbf{n} &= -\left(\alpha^k B_k^i + \nabla_s^i \beta\right)\mathbf{e}_i,\\
\delta g_{ij} &= \nabla_{s,i}\alpha_j + \nabla_{s,j}\alpha_i - 2\beta B_{ij},\\
\delta g^{ij} &= -\nabla_s^i \alpha^j - \nabla_s^j \alpha^i + 2\beta B^{ij},\\
\delta B_{ij} &= \left(\nabla_{s,i}\nabla_{s,j} - 2H B_{ij} + K g_{ij}\right)\beta + B_{ik}\nabla_{s,j}\alpha^k + B_{kj}\nabla_{s,i}\alpha^k + \alpha^k \nabla_{s,k} B_{ij},\\
\delta g &= g\left(2\nabla_{s,i}\alpha^i - 4H\beta\right),
\end{aligned}$$

$$\begin{aligned}
\delta\sqrt{g} &= \sqrt{g}\left(\nabla_{s,i}\alpha^i - 2H\beta\right),\\
\delta H &= \left(2H^2 - K\right)\beta + \frac{1}{2}\Delta_s \beta + \alpha^k \nabla_{s,k} H,\\
\delta K &= (2H\delta_i^j - B_i^j)\nabla_{s,j}\nabla_s^i \beta + 2HK\beta + \alpha^k \nabla_{s,k} K\\
&= \overline{\Delta}_s \beta + 2HK\beta + \alpha^k \nabla_{s,k} K.
\end{aligned}$$

The surface Laplacian is $\Delta_s \equiv \nabla_s^2 \equiv (\sqrt{g})^{-1}\partial_i(\sqrt{g}g^{ij}\partial_j)$ and $\overline{\Delta}_s \equiv (\sqrt{g})^{-1}\partial_i\left(\sqrt{g}(2Hg^{ij} - B^{ij})\partial_j\right)$ and $i, j = 1, 2$ throughout.

To illustrate the derivation of these, consider the first two.

$$\begin{aligned}
\delta \boldsymbol{e}_j = \frac{\partial \delta \boldsymbol{x}}{\partial u^j} &= \left(\frac{\partial \alpha^i}{\partial u^j}\boldsymbol{e}_i + \alpha^i \frac{\partial \boldsymbol{e}_i}{\partial u^j}\right) + \left(\frac{\partial \beta}{\partial u^j}\boldsymbol{n} + \beta \frac{\partial \boldsymbol{n}}{\partial u^j}\right)\\
&= \left(\frac{\partial \alpha^i}{\partial u^j}\boldsymbol{e}_i + \alpha^i \Gamma_{ij}^k \boldsymbol{e}_k + \alpha^i B_{ij}\boldsymbol{n}\right) + \left(\frac{\partial \beta}{\partial u^j}\boldsymbol{n} - \beta B_j^i \boldsymbol{e}_i\right)\\
&= \left(\nabla_{s,j}\alpha^i - \beta B_j^i\right)\boldsymbol{e}_i + \left(\frac{\partial \beta}{\partial u^j} + \alpha^i B_{ij}\right)\boldsymbol{n},
\end{aligned}$$

and for $\delta \boldsymbol{n}$

$$\begin{aligned}
\delta \boldsymbol{n} &= -\left(\boldsymbol{n} \cdot \delta \boldsymbol{e}_j\right)\boldsymbol{e}^j\\
&= -\left(\frac{\partial \beta}{\partial u^j} + \alpha^i B_{ij}\right)\boldsymbol{e}^j.
\end{aligned}$$

Now consider an integral that involves a general quantity Q on the surface.

$$\int_S Q\, dS$$

where $dS = \sqrt{g}\, du^1 du^2$ is the area element and Q is some sufficiently smooth function defined on the surface. Now consider a variation of the surface, and assume that Q may be dependent upon the geometry. Then we have

$$\begin{aligned}
\frac{\delta}{\delta \boldsymbol{x}}\int_S Q\, dS &= \int_S \frac{\delta}{\delta \boldsymbol{x}}\left(Q\sqrt{g}\right) du^1 du^2\\
&= \int_S Q \frac{1}{2}(g^{ij}\delta g_{ij})\sqrt{g} du^1 du^2 + \int_S \frac{\delta Q}{\delta \boldsymbol{x}} \cdot \delta \boldsymbol{x}\sqrt{g} du^1 du^2\\
&= \int_S Q\, \nabla_s \cdot \delta \boldsymbol{x}\, \sqrt{g} du^1 du^2 + \int_S \frac{\delta Q}{\delta \boldsymbol{x}} \cdot \delta \boldsymbol{x}\sqrt{g} du^1 du^2 \qquad (20)\\
&= \int_S \left(Q\nabla_s \cdot \delta \boldsymbol{x} + \frac{\delta Q}{\delta \boldsymbol{x}} \cdot \delta \boldsymbol{x}\right) dS\\
&= \int_S \left(\left(-\nabla_s Q - 2HQ\boldsymbol{n}\right) \cdot \delta \boldsymbol{x} + \frac{\delta Q}{\delta \boldsymbol{x}} \cdot \delta \boldsymbol{x}\right) dS
\end{aligned}$$

From this we see that there are two types of quantities, those with values that depend on variations of the surface such as the mean

curvature, and those that are merely advected as the surface moves, such as the bending modulus, which we call Lagrangian quantities.

Derivation of forces with variable bending moduli

Consider a Helfrich–Canham functional with variable k_c and k_G. We will assume that although k_c and k_G are functions of position, they are merely advected with any deformation. In other words they are treated like Lagrangian quantities.

First consider the term with k_c. Using Eq. (20) with $Q = \frac{1}{2}k_c(2H - C_0)^2$ yields,

$$\delta E_c = \int k_c(2H - C_0)\frac{\delta H}{\delta \boldsymbol{x}} \cdot \delta \boldsymbol{x} + \left(-\frac{1}{2}\nabla_s k_c(2H - C_0)^2 - k_c H(2H - C_0)^2 \boldsymbol{n}\right) \cdot \delta \boldsymbol{x} dS$$

where we have used the fact that $\delta k_c = 0$ by assumption. Substituting the formula for δH above, using the partial integration formula twice, and simplifying yields a formula,

$$\frac{\delta E_c}{\delta \boldsymbol{x}} = \left[\Delta_s\left[k_c(2H - C_0)\right] + k_c(2H - C_0)\left(2H^2 - 2K + HC_0\right)\right]\boldsymbol{n} - \left[\frac{1}{2}(2H - C_0)^2\nabla_s k_c\right]$$

The resulting forces due to this term are $\boldsymbol{f}_c = -\frac{\delta E_c}{\delta \boldsymbol{x}}$.

Next consider $k_G(u^1, u^2)$ as a Lagrangian function as above and consider the variation of

$$E_K = \int_S k_G K \, dS.$$

Since this force is rarely discussed in the literature, we provide a more detailed calculation. Here $Q = k_G K$, thus, upon differentiation we obtain

$$\begin{aligned}\delta E_K &= \int_S \left(\left(-\nabla_s Q - 2HQ\boldsymbol{n}\right) \cdot \delta \boldsymbol{x} + \frac{\delta Q}{\delta \boldsymbol{x}} \cdot \delta \boldsymbol{x}\right) dS \\ &= \int_S \left[-\nabla_s\left(k_G K\right) - 2k_G H K \boldsymbol{n}\right] \cdot \delta \boldsymbol{x} \\ &\quad + k_G\left((2H\delta_i^j - B_i^j)\nabla_{s,j}\nabla_s^i \beta + 2\beta K H + \alpha^i \nabla_{s,i} K\right) dS \\ &= \int_S -K\nabla_s k_G \cdot \delta \boldsymbol{x} + k_G\left((2H\delta_i^j - B_i^j)\nabla_{s,j}\nabla_s^i \beta\right) dS\end{aligned}$$

To further simplify the second term, consider the divergence integral,

$$\int_S \nabla_s^i k_G\left((2H\delta_i^j - B_i^j)\nabla_{s,j}\beta\right) dS = 0.$$

which is 0 due to the divergence theorem, and since there is no normal component of the vector $k_G(2H\delta_i^j + B_i^j)\nabla_{s,j}\beta$. Upon using the product rule for covariant differentiation,

$$\int_S k_G\left((2H\delta_i^j - B_i^j)\nabla_{s,j}\nabla_s^i \beta\right) dS + \int_S \nabla_s^i\left[k_G(2H\delta_i^j - B_i^j)\right]\nabla_{s,j}\beta dS = 0$$

where the first term is the normal component of δE_K. Next, note that the Gauss–Codazzi formula implies that,

$$\nabla_{s,i} B_j^i = \nabla_{s,j} B_i^i = 2\nabla_{s,j} H,$$

to obtain

$$\nabla_{s,i}\left(2H\delta_j^i - B_j^i\right) = \nabla_{s,j}(2H - 2H) = 0$$

This allows us to simplify

$$\int_S \nabla_s^i\left[k_G(2H\delta_i^j - B_i^j)\right]\nabla_{s,j}\beta dS = \int_S \left[(2H\delta_i^j - B_i^j)\nabla_s^i k_G\right]\nabla_{s,j}\beta dS.$$

A second use of the partial integration formula yields

$$\int_S \left[(2H\delta_i^j - B_i^j)\nabla_s^i k_G\right]\nabla_{s,j}\beta dS + \int_S \left[\nabla_{s,j}(2H\delta_i^j - B_i^j)\nabla_s^i k_G\right]\beta dS = 0.$$

Combining this last term with the tangential terms yields

$$\frac{\delta E_K}{\delta \boldsymbol{x}} = -K\nabla_s k_G + \left[\nabla_{s,j}(2H\delta_i^j - B_i^j)\nabla_s^i k_G\right]\boldsymbol{n} = -K\nabla_s k_g + \overline{\Delta}_s k_g.$$

The modified Laplacian term can be represented concisely in vector form by defining tensors

$$\boldsymbol{W} = B_j^i \boldsymbol{e}_i \boldsymbol{e}^j, \qquad \boldsymbol{I}_s = \boldsymbol{e}^i \boldsymbol{e}_i$$

where $\boldsymbol{I}_s$ is a surface projection which projects an arbitrary vector at point $\boldsymbol{x} \in S$ into the tangent space of S at $\boldsymbol{x}$. Thus, we can define the tangential and normal force components:

$$\boldsymbol{f}^t = \boldsymbol{I}_s \boldsymbol{f}, \qquad f^n = \boldsymbol{n} \cdot \boldsymbol{f} = \boldsymbol{n} \cdot (\boldsymbol{I} - \boldsymbol{I}_s)\boldsymbol{f}$$

For the Gaussian curvature force, we have that

$$f^n = (2H\boldsymbol{I}_s - \boldsymbol{W}) : \nabla_s \nabla_s k_G$$
$$\boldsymbol{f}^t = K\nabla_s k_G.$$

Interchange of the derivative is possible here due to the result above that $\nabla_{s,i}(2H\delta_j^i - B_j^i) = 0$.

Appendix B. Numerical methods

Method of regularized Stokeslets

The solution to Stokes equations in the presence of a boundary force can be written in terms of a convolution with a tensor-valued Green's function, $\boldsymbol{U}$ as [58]

$$\boldsymbol{u}(\boldsymbol{x}, t) = \int_S \boldsymbol{U}(\boldsymbol{x} - \boldsymbol{y}(t))\boldsymbol{f}(\boldsymbol{y}(t), t) dS.$$

where $\boldsymbol{U}$ satisfies (summation implied)

$$\mu\frac{\partial^2 U_{ij}}{\partial x_k \partial x_k} - \frac{\partial P_i}{\partial x_j} = \delta_{ij}\delta(\boldsymbol{x} - \boldsymbol{y})$$
$$\frac{\partial U_{ik}}{\partial x_k} = 0$$

where $i, j, k = 1, 2, 3$. The term $\boldsymbol{P}$ is the Green's function pressure solution for a point force. These Green's functions are known analytically,

$$U_{ij}(\boldsymbol{x}) = \frac{1}{8\pi\mu}\left(\frac{\delta_{ij}}{|\boldsymbol{x}|} + \frac{x_i x_j}{|\boldsymbol{x}|^3}\right), \qquad P_i(\boldsymbol{x}) = \frac{1}{4\pi}\frac{x_i}{|\boldsymbol{x}|^3}.$$

Thus, given our computation of $\boldsymbol{f}$ above, we can compute the integral in theory. One issue is that the kernel $\boldsymbol{U}$ is weakly singular near $\boldsymbol{x} = \boldsymbol{y}$, thus standard quadrature cannot be applied. One way of removing this difficulty is to first smooth out $\boldsymbol{U}$ by convolving it with some smooth approximate Dirac delta function, e.g.

$$\boldsymbol{U}_\delta = \int_S \boldsymbol{U}(\boldsymbol{x} - \boldsymbol{y})\zeta_\delta(\boldsymbol{y}) d\Omega,$$

and this is the essence behind the method of regularized Stokeslets. Using the choice of ζ_δ introduced in [57],

$$\zeta_\delta(r) = \frac{15\delta^4}{8\pi(r^2 + \delta^2)^{7/2}},$$

we now compute $\boldsymbol{u}(\boldsymbol{x}, t)$ with the modified kernel.

In order to compute the integral, we note the output of the finite element methods above typically yields

$$\boldsymbol{f}_i^h = \int_{S^h} \boldsymbol{f} \cdot \boldsymbol{\phi}_i dS$$

where $\boldsymbol{\phi}_i$ is a basis function in the discretization. The integral $\int_S \boldsymbol{U}_\delta(\boldsymbol{x} - \boldsymbol{y})\boldsymbol{f}(\boldsymbol{y}) dS$ is then approximated as

$$\boldsymbol{u}(\boldsymbol{x}) = \sum_{i=1}^{N^h} \boldsymbol{U}_\delta(\boldsymbol{x} - \boldsymbol{y}_i^h)\boldsymbol{f}_i^h$$

since $\boldsymbol{f}_i^h$ already includes a weighting factor that accounts for the local surface area. This approach can be understood as a form of mass-lumping in the sense that rather than compute the integral over the element of $\boldsymbol{U}_\delta(\boldsymbol{x} - \boldsymbol{y})\boldsymbol{f}(\boldsymbol{y})$, we instead integrate $\boldsymbol{f}(\boldsymbol{y})$ first, and then simply multiply by an individual value of $\boldsymbol{U}_\delta(\boldsymbol{x} - \boldsymbol{y})$.

Computer implementation details and mesh adaptivity

The simulations were run in Matlab. The finite element implementation was done using FELICITY [59]. Mesh generation was also done using FELICITY and adaptation was done using a Delaunay-frontal sweeping method implemented in the Jigsaw meshing library [60]. Upon adaptation, geometric consistency between the new mesh and the associated mean-curvature approximation was enforced via the algorithm in [47]. By geometric consistency we mean that the identity

$$-\int_{S^h} \nabla_s \boldsymbol{x}^h : \nabla_s \boldsymbol{\phi} dS = \int_{S^h} \boldsymbol{H}^h \cdot \boldsymbol{\phi} dS \qquad \forall \boldsymbol{\phi} \in \mathcal{P}^2(S^h)$$

was enforced on the new mesh. To achieve geometric consistency, the procedure is to first produce a tentative remeshing of S^h, and then compute the curvature, $\boldsymbol{H}^h_{\text{new}}$. The new positions, $\boldsymbol{x}^h_{\text{new}}$ are then found by inverting the Laplace–Beltrami operator while preserving area and volume via Lagrange-multiplier constraints. For closed surfaces, Δ_s has a null-space consisting of constant functions. Thus, prior to inverting Δ_s, the mean value of $\boldsymbol{H}^h$ is subtracted off, and after solution, the mean value of $\boldsymbol{x}^h_{\text{new}}$ is set to 0 to avoid spurious translational motion when refining. If the center of volume of S^h is nonzero prior to remeshing, then after remeshing S^h_{new} can be translated accordingly.

After remeshing, quantities, such as the area strain $\epsilon_A = \frac{\sqrt{g}-\sqrt{g_0}}{\sqrt{g_0}}$, that are not functions solely of the current geometry are interpolated from the old mesh to the new mesh.

In addition to remeshing, spatially adaptive refinement is beneficial when the curvature in certain portions of the surface becomes large enough such that the shape of the surface is not well represented by the mesh resolution. Adaptivity was achieved by approximating the largest magnitude principal curvature. To find this note that the mean curvature and Gaussian curvature are related to the principal curvatures, κ_1 and κ_2 by

$$K = \kappa_1\kappa_2, \quad H = \frac{1}{2}(\kappa_1 + \kappa_2).$$

Solving for κ_1 and κ_2 yields

$$\kappa_1 = H + \sqrt{H^2 - K}$$
$$\kappa_2 = H - \sqrt{H^2 - K}.$$

In practice, we take the absolute value of $H^2 - K$ since numerical error can cause this quantity to become slightly negative on occasion. Remeshing is done by setting the maximum element diameter to be bounded by a decreasing function of $\kappa = \max\left(|\kappa_1|, |\kappa_2|\right)$. In our case, we found that the function $\min\left(\frac{1}{\kappa^2}, \kappa/4.5\right)$ worked well, but this is heuristic and found via trial and error.

To run the simulation, we start in each case with a timestep of $\delta t = 10^{-10}$ and allow δt to grow over time to a maximum $\delta t = 2 \times 10^{-4}$. This allows us to capture any fast dynamics that are known to arise in Helfrich flows, but also allows us to capture longer time scales with fairly reasonable computational cost. Nonetheless, larger forces and more extreme deformations may necessitate smaller timesteps, finer spatial discretization, and hence more costly simulations. The transition between the small and large time steps was done by multiplying $\delta t_n = \delta t_{n-1} \times c_n$ until $\delta t_n \geq 2 \times 10^{-4}$. The amplification factor, c_n is bounded by 1.15, but depends on the how rapidly the membrane position and curvature change between time steps in order to ensure that no instabilities arise. As a precaution, we also temporarily reduce δt by a factor of 10 after remeshing, although this was probably not needed.

Lastly, to compute the local area elements, consider the set of nodal points, $\boldsymbol{x}$ in the P_2-Lagrange element mesh. Now subdivide each triangular element in the original discretization into 4 subtriangles. The value of $\sqrt{g(\boldsymbol{x})}$ associated with each $\boldsymbol{x}$ is then computed as 1/3 the sum of the areas of each subtriangle which contains $\boldsymbol{x}$ as a vertex.

References

[1] C.D. Paul, P. Mistriotis, K. Konstantopoulos, Cancer cell motility: lessons from migration in confined spaces, Nat. Rev. Cancer 17 (2) (2017) 131.

[2] H.G. Othmer, Eukaryotic cell motility from crawlers to swimmers, WIRES Comp. Mol. Sci. (2018) 1–24, http://dx.doi.org/10.1002/wcms.1376.

[3] M. Bergert, A. Erzberger, R.A. Desai, I.M. Aspalter, A.C. Oates, G. Charras, G. Salbreux, E.K. Paluch, Force transmission during adhesion-independent migration, Nat. Cell Biol. (2015).

[4] Q. Wang, H.G. Othmer, Computational analysis of amoeboid swimming at low Reynolds number, J. Math. Biol. 72 (2015) 1893–1926.

[5] T. Lämmermann, B.L. Bader, S.J. Monkley, T. Worbs, R. Wedlich-Söldner, K. Hirsch, M. Keller, R. Förster, D.R. Critchley, R. Fässler, et al., Rapid leukocyte migration by integrin-independent flowing and squeezing, Nature 453 (7191) (2008) 51.

[6] Q. Wang, H.G. Othmer, Analysis of a model microswimmer with applications to blebbing cells and mini-robots, J. Math. Biol. 76 (7) (2018) 1699–1763.

[7] R.J. Petrie, K.M. Yamada, Multiple mechanisms of 3d migration: the origins of plasticity, Curr. Opin. Cell Biol. 42 (2016) 7–12.

[8] H. Zhang, D. Wessels, P. Fey, K. Daniels, R.L. Chisholm, D.R. Soll, Phosphorylation of the myosin regulatory light chain plays a role in motility and polarity during dictyostelium chemotaxis, J. Cell Sci. 115 (Pt 8) (2002) 1733–1747.

[9] P.R. O'Neill, J.A. Castillo-Badillo, X. Meshik, V. Kalyanaraman, K. Melgarejo, N. Gautam, Membrane flow drives an adhesion-independent amoeboid cell migration mode, Dev. Cell 46 (1) (2018) 9–22.

[10] J.D. Howe, N.P. Barry, M.S. Bretscher, How do amoebae swim and crawl? PLoS One 8 (9) (2013) e74382.

[11] H. Wu, M. Avila Ponce de León, H.G. Othmer, Getting in shape and swimming: the role of cortical forces and membrane heterogeneity in eukaryotic cells, J. Math. Biol. (2018) 1–32.

[12] J. Dai, H.P. Ting-Beall, R.M. Hochmuth, M.P. Sheetz, M.A. Titus, Myosin I contributes to the generation of resting cortical tension, Biophys. J. 77 (2) (1999) 1168–1176.

[13] R. Merkel, R. Simson, D.A. Simson, M. Hohenadl, A. Boulbitch, E. Wallraff, E. Sackmann, A micromechanic study of cell polarity and plasma membrane cell body coupling in dictyostelium, Biophys. J. 79 (2) (2000) 707–719.

[14] M. Fritzsche, C. Erlenkämper, E. Moeendarbary, G. Charras, K. Kruse, Actin kinetics shapes cortical network structure and mechanics, Sci. Adv. 2 (4) (2016) e1501337.

[15] F.M. Hochmuth, J.Y. Shao, J. Dai, M.P. Sheetz, Deformation and flow of membrane into tethers extracted from neuronal growth cones, Biophys. J. 70 (1) (1996) 358–369.

[16] J. Dai, M.P. Sheetz, Membrane tether formation from blebbing cells, Biophys. J. 77 (6) (1999) 3363–3370.

[17] P. Chugh, A.G. Clark, M.B. Smith, D.A.D. Cassani, K. Dierkes, A. Ragab, P.P. Roux, G. Charras, G. Salbreux, E.K. Paluch, Actin cortex architecture regulates cell surface tension, Nat. Cell Biol. 19 (6) (2017) 689–697.

[18] R.J. Hawkins, R. Poincloux, O. Bénichou, M. Piel, P. Chavrier, R. Voituriez, Spontaneous contractility-mediated cortical flow generates cell migration in three-dimensional environments, Biophys. J. 101 (5) (2011) 1041–1045.

[19] G. Salbreux, G. Charras, E. Paluch, Actin cortex mechanics and cellular morphogenesis, Trends Cell Biol. 22 (10) (2012) 536–545.

[20] M. Kapustina, T.C. Elston, K. Jacobson, Compression and dilation of the membrane-cortex layer generates rapid changes in cell shape, J. Cell Biol. 200 (1) (2013) 95–108.

[21] M. Bovellan, Y. Romeo, M. Biro, A. Boden, P. Chugh, A. Yonis, M. Vaghela, M. Fritzsche, D. Moulding, R. Thorogate, et al., Cellular control of cortical actin nucleation, Curr. Biol. 24 (14) (2014) 1628–1635.

[22] E. Moeendarbary, G. Charras, Cell mechanics: hydraulic cracking, Nature Mater. 14 (3) (2015) 268–269.

[23] H. Wu, H. Othmer, Cortical-tension-driven amoeboid swimming. Unpublished notes, 2018.

[24] Y.J. Liu, M. Le Berre, F. Lautenschlaeger, P. Maiuri, A. Callan-Jones, M. Heuzé, T. Takaki, R. Voituriez, M. Piel, Confinement and low adhesion induce fast amoeboid migration of slow mesenchymal cells, Cell 160 (4) (2015) 659–672.

[25] P. Chengappa, K. Sao, T.M. Jones, R.J. Petrie, Intracellular Pressure: A Driver of Cell Morphology and Movement, in: Int. Rev. Cell Mol. Biol., vol. 337, Elsevier, 2018, pp. 185–211.

[26] G.T. Charras, J.C. Yarrow, M.A. Horton, L. Mahadevan, T.J. Mitchison, Non-equilibration of hydrostatic pressure in blebbing cells, Nature 435 (7040) (2005) 365–369.

[27] J.Y. Tinevez, U. Schulze, G. Salbreux, J. Roensch, J.F. Joanny, E. Paluch, Role of cortical tension in bleb growth, Proc. Natl. Acad. Sci. USA 106 (44) (2009) 18581–18586.

[28] J.F. Joanny, J. Prost, Active gels as a description of the actin–myosin cytoskeleton, HFSP J. 3 (2) (2009) 94–104.

[29] J. Prost, F. Jülicher, J.F. Joanny, Active gel physics, Nat. Phys. 11 (2) (2015) 111.

[30] F. Jülicher, S.W. Grill, G. Salbreux, Hydrodynamic theory of active matter, Rep. Progr. Phys. 81 (7) (2018) 076601.

[31] U. Seifert, K. Berndl, R. Lipowsky, Shape transformations of vesicles: phase diagram for spontaneous-curvature and bilayer-coupling models, Phys. Rev. A 44 (1991) 1182–1202.
[32] U. Seifert, Configurations of fluid membranes and vesicles, Adv. Phys. 46 (1997) 13–137.
[33] Z.C. Tu, Z.C. Ou-Yang, Recent theoretical advances in elasticity of membranes following helfrich's spontaneous curvature model, Adv. Colloid Interface Sci. 208 (2014) 66–75.
[34] A. Guckenberger, S. Gekle, Theory and algorithms to compute helfrich bending forces: A review, J. Phys. Condens. Matter 29 (20) (2017) 203001.
[35] L. Mesarec, W. Góźdź, A. Iglič, V. Kralj-Iglič, E.G. Virga, S. Kralj, Normal red blood cells' shape stabilized by membrane's in-plane ordering, Sci. Rep. 9 (1) (2019) 1–11.
[36] T.J. Willmore, An Introduction to Differential Geometry, Oxford University Press, 1959.
[37] J.W. Barrett, H. Garcke, R. Nürnberg, Parametric approximation of willmore flow and related geometric evolution equations, SIAM J. Sci. Comput. 31 (1) (2008) 225–253.
[38] P.B. Canham, The minimum energy of bending as a possible explanation of the biconcave shape of the human red blood cell, J. Theoret. Biol. 26 (1) (1970) 61–76.
[39] W. Helfrich, Elastic properties of lipid bilayers: theory and possible experiments, Z. Naturforsch. C 28 (11–12) (1973) 693–703.
[40] A. Diz-Muñoz, K. Thurley, S. Chintamen, S.J. Altschuler, L.F. Wu, D.A. Fletcher, O.D. Weiner, Membrane tension acts through PLD2 and mTORC2 to limit actin network assembly during neutrophil migration, PLoS Biol. 14 (6) (2016) e1002474.
[41] Z.C. Ou-Yang, W. Helfrich, Bending energy of vesicle membranes: general expressions for the first, second, and third variation of the shape energy and applications to spheres and cylinders, Phys. Rev. A 39 (10) (1989) 5280.
[42] R. Capovilla, J. Guven, J.A. Santiago, Deformations of the geometry of lipid vesicles, J. Phys. A Math. 36 (23) (2003) 6281.
[43] M. Thiébaud, C. Misbah, Rheology of a vesicle suspension with finite concentration: A numerical study, Phys. Rev. E 88 (6) (2013) 062707.
[44] H. Wu, M. Thiébaud, W.-F. Hu, A. Farutin, S. Rafaï, M.-C. Lai, P. Peyla, C. Misbah, Amoeboid motion in confined geometry, Phys. Rev. E 92 (5) (2015) 050701.
[45] H. Wu, A. Farutin, W.F. Hu, M. Thiébaud, S. Rafaï, P. Peyla, M.C. Lai, C. Misbah, Amoeboid swimming in a channel, Soft Matter 12 (36) (2016) 7470–7484.
[46] G. Dziuk, C.M. Elliott, Finite element methods for surface PDEs, Acta Numer. 22 (2013) 289–396.
[47] A. Bonito, R.H. Nochetto, M.S. Pauletti, Parametric fem for geometric biomembranes, J. Comput. Phys. 229 (9) (2010) 3171–3188.
[48] L.C. Evans, Partial Differential Equations, Graduate Studies in Mathematics, 19, American Mathematical Society, 1998.
[49] R.M. Hochmuth, Micropipette aspiration of living cells, J. Biomech. 33 (1) (2000) 15–22.
[50] R. Alert, J. Casademunt, J. Brugués, P. Sens, Model for probing membrane-cortex adhesion by micropipette aspiration and fluctuation spectroscopy, Biophys. J. 108 (8) (2015) 1878–1886.
[51] G. Dziuk, Computational parametric willmore flow, Numer. Math. 111 (1) (2008) 55.
[52] J.W. Barrett, H. Garcke, R. Nürnberg, Parametric approximation of willmore flow and related geometric evolution equations, SIAM J. Sci. Comput. 31 (1) (2008) 225–253.
[53] D. Steigmann, Fluid films with curvature elasticity, Arch. Ration. Mech. Anal. 150 (2) (1999) 127–152.
[54] B. Stinner, A. Dedner, A. Nixon, A finite element method for a fourth order surface equation with application to the onset of cell blebbing, Front. Appl. Math. Stat. 6 (2020) 21.
[55] J.E. Marsden, T.J.R. Hughes, Mathematical Foundations of Elasticity, Courier Corporation, 1994.
[56] R. Cortez, The method of regularized Stokeslets, SIAM J. Sci. Comput. 23 (4) (2001) 1204–1225.
[57] R. Cortez, L. Fauci, A. Medovikov, The method of regularized Stokeslets in three dimensions: analysis, validation, and application to helical swimming, Phys. Fluids 17 (3) (2005) 031504.
[58] C. Pozrikidis, Boundary Integral and Singularity Methods for Linearized Viscous Flow, Cambridge University Press, 1992.
[59] S.W. Walker, Felicity: A matlab/C++ toolbox for developing finite element methods and simulation modeling, SIAM J. Sci. Comput. 40 (2) (2018) C234–C257.
[60] D. Engwirda, Conforming restricted delaunay mesh generation for piecewise smooth complexes, Procedia Eng. 163 (2016) 84–96.